SAND2021-13491C

22PFL-0207

Numerical and Experimental Studies of a Novel Dimpled Stepped-Lip Piston Design on Turbulent Flow Development in a Medium-Duty Diesel Engine

Author, co-author (Do NOT enter this information. It will be pulled from participant tab in MyTechZone)

Affiliation (Do NOT enter this information. It will be pulled from participant tab in MyTechZone)

Abstract

Spray-wall interactions in diesel engines have a strong influence on turbulent flow evolution and mixing, which influences the engine's thermal efficiency and pollutant-emissions behavior. Previous optical experiments and numerical investigations of a stepped-lip diesel piston bowl focused on how spray-wall interactions influence the formation of squish-region vortices and their sensitivity to injection timing. Such vortices are stronger and longer-lived at retarded injection timings and are correlated with faster late-cycle heat release and soot reductions, but are weaker and shorter-lived as injection timing is advanced. Computational fluid dynamics (CFD) simulations predict that piston bowls with more space in the squish region can enhance the strength of these vortices at near-TDC injection timings, which is hypothesized to further improve peak thermal efficiency and reduce emissions. The dimpled stepped-lip (DSL) piston is such a design.

In this study, the in-cylinder flow is simulated with a DSL piston to investigate of the effects of dimple geometry parameters on squish-region vortex formation via a design sensitivity study. The rotational energy and size of the squish-region vortices are quantified. The results suggest that the DSL piston is capable of enhancing vortex formation compared to the stepped-lip piston at near-TDC injection timings. The sensitivity study led to the design of an improved DSL bowl with shallower, narrower, and steeper-curved dimples that are further out into the squish region, which enhances predicted vortex formation with 27% larger and 44% more rotationally energetic vortices compared to the baseline DSL bowl. Engine experiments with the baseline DSL piston demonstrate that it can reduce combustion duration and improve thermal efficiency by as much as 1.4% with main injection timings near TDC, with 69% increased soot emissions, but no penalty in NOx emissions.

Introduction

The shape of a diesel piston bowl strongly influences the engine's thermal efficiency and emissions characteristics, as it affects the spray-wall interactions and fuel-air mixing processes. Studies have shown, for example, that a stepped-lip (SL) piston, also known as a chamfered-lip piston, leads to enhanced mixing-controlled heat release rates with improved thermal efficiency [1-6], but not all studies found similar thermal efficiency gains [7, 8]. Improvements in thermal efficiency were partly attributed to lower heat transfer losses [5, 9-11], although other studies have found that wall heat losses were not always the cause [4, 12]. Other causes are improved fuel-air mixing with enhanced air utilization, which also reduces smoke emissions [1, 4, 6, 13-16]. Enhancement of fuel-air mixing is attributed to the formation of a dual vortex structure as fuel spray interacts with the stepped-lip piston surface. [4, 6, 13, 17, 18]. Busch et al. [3, 19] used CFD to predict enhancement of vortices in the squish region with the stepped-lip piston. Evidence of such vortices was observed previously in an optical engine study [18] and was correlated with improved efficiency and smoke emissions at retarded injection timings as they enhance mixing-controlled heat release. However, as injection timing was advanced towards TDC, the strength and longevity of such vortices diminished, reducing the efficiency benefits [3, 4, 18, 19].

The stepped-lip piston design was reported as early as 2007 [16], which achieved reduced soot emissions and slight improvements in fuel efficiency using this piston design. In the same year, a patent was filed by Hino Motors [2] which features the stepped-lip piston design. They show a portion of the injected fuel is directed upwards by the stepped surface as it is also moving radially outwards into the squish region. Two counter-rotating vortices form to increase fuel-air mixing in the combustion chamber. In 2011, a patent was filed by Ricardo for a stepped-lip piston design known as the Twin Vortex Combustion System [14], with an annular lip that protrudes further out into the combustion chamber [20]. The annular lip is used to increase the residence time of the swirling motion when fuel is injected and directed into the lower part of the combustion chamber, thereby increasing fuel-air mixing. In the same year, Ford engineered a chamfered re-entrant bowl [9] featuring a near-vertical step. Metal engine experiments show improvements in emissions and fuel consumption, which they attributed to better air utilization in the squish region and a reduction in the total surface area leading to less wall heat transfer [1]. In 2013, Doosan developed the Ultra-Low Particulate Combustion strategy featuring a tapered step, effectively splitting the combustion chamber into two combustion zones [6]. Their experiments show that the stepped-lip piston enhanced the soot-NOx tradeoff with optimized spray targeting. In 2016, Daimler announced their stepped-lip piston design for Mercedes-Benz with improved air utilization, higher efficiency, and lower emissions with reduced heat losses [21].

Piston bowl designs have continued to evolve beyond the stepped-lip piston design. A double stepped-lip piston was simulated and its bowl geometry was optimized through a design of experiment study [22].The optimal piston has a slightly lower bowl volume and 0.05 higher compression ratio than the baseline piston. Experiments with the optimized piston revealed increased torque and reduced fuel consumption, likely due to higher squish velocity leading to better fuel-air mixing. Recently, a patent was filed for such a double stepped-lip design, which shows decreased soot with maintained NOx and hydrocarbon emissions as fuel-air mixing is improved in the squish region, with lower liner soot-in-oil [23]. Another novel piston design is the Volvo wave piston, which features radial waves in the piston bowl to improve air utilization and fuel efficiency at high loads [24, 25]. Such waves were also featured in a stepped-lip piston to further improve air utilization at high loads [26]. An annular bump ring has also been used in to introduce additional vortices in the combustion chamber to enhance mixing [27]. A novel dimpled-stepped lip (DSL) piston geometry was designed and simulated with CFD in a small-bore diesel research engine and was shown to improve vortex formation even with near-TDC injection timing [3], which was therefore hypothesized to increase thermal efficiency and reduce soot emissions. The objective of this work is to test this hypothesis.

This paper presents a CFD and experimental study in a medium-duty diesel research engine with a DSL piston to analyze the effects of dimple geometry parameters on squish-region vortex formation. In the first part of the study, the CFD simulations are presented. The dimple parameters are systematically varied in a design sensitivity study. The spatial distribution of factors affecting radial momentum and vorticity are qualitatively compared against the simulation results from the same engine with a baseline stepped-lip piston design. In addition, the rotational energy and size of these vortices are quantified. In the second part of the study, the performance and emissions of a single-cylinder diesel research engine equipped with a DSL piston are compared to the baseline engine with a stepped-lip piston for a part-load operating point.

Methodology

Simulation Setup

The engine simulated is the Sandia single-cylinder, medium-duty diesel research engine, based on the Ford 6.7L combustion system [28]. This four-valve engine is built with the production piston/rod assembly and fuel injector, with bore and stroke equal to that of the production engine. Table 1 contains the engine specifications. Simulations are carried out in the FRESCO CFD solver [29]. Turbulence closure is modeled using the generalized renormalization group (GRNG) k-ε model [30], with near-wall flow and heat transfer modeled using Han and Reitz's law-of-the-wall model [31, 32]. Fuel injection and spray phenomena are modeled with a Lagrangian-Droplet/Eulerian-Fluid approach, and have been validated and optimized against Engine Combustion Network (ECN) Spray A data [33, 34] without further tuning due to good agreement with experimental liquid and fuel vapor data [35]. Further details on the sub-models for the spray modeling can be found in [3]. Figure 1 shows the computational domain of the engine, where a body-fitted unstructured hexahedral mesh is used for the full engine model. It is comprised of approximately 1 million cells at bottom dead center. It was found previously that modeling the full engine geometry with non-axisymmetric cylinder head features was needed to predict accurate flow evolution in a small-bore diesel engine with a stepped-lip piston [36].

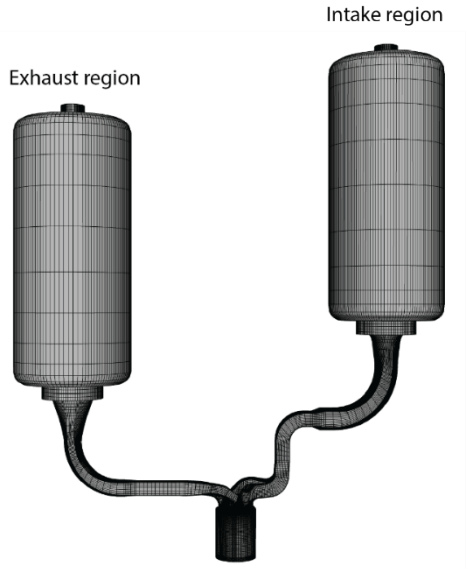

Figure 1. Computational domain.

Table 1. Engine specifications.

Bore	99 mm
Stroke	108 mm
Displacement volume	831.35 mL

Compression ratio	16.35:1
Injector nozzle holes	8-hole piezo
Nozzle hole radial position	1.365 mm
Nozzle hole axial position from fire deck	1.114 mm
Injector protrusion depth	2.5 mm

A multi-cycle RANS non-combusting simulation is performed by starting at exhaust valve opening (106 crank angle degrees (CAD) after top dead center of the compression stroke (aTDCc) in cycle 0, initialized with a swirl ratio of 1.99. Then, cold flow is simulated in cycle 1 to remove any initial condition bias and to establish the flow, and fuel is injected in cycle 2, following the same procedures as [3]. Boundary conditions are listed in Table 2. A dual-pilot, single-main injection strategy with constant dwell between each injection is used and block-shifted to match two injection timings based on experiments in order to analyze effects of injection timing on spray-wall interactions and flow evolution. Here, the simulations are performed in the medium-duty diesel engine with an early, near-TDC injection timing, and an intermediate injection timing as shown in Table 3. For the purposes of the simulations, the main fuel injection quantity is unchanged between the two injection timings. The simulated injection profiles are shown in

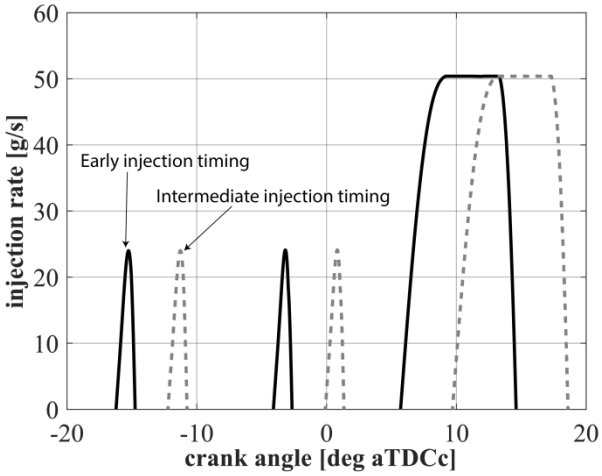

Figure 2.

Table 2. Boundary conditions for the simulation.

Engine speed	1600 RPM
Piston surface temperature	486 K
Head surface temperature	486 K
Liner surface temperature	476 K
Intake pressure (constant, applied at intake surge tank entrance)	137 kPa
Intake plenum temperature	468.1 K
Intake port surface temperature	375 K
Intake valves temperature	416 K
Exhaust valves temperature	446 K
Exhaust port surface temperature	456 K
Exhaust plenum temperature	468.1 K
Exhaust pressure (constant, applied at exhaust surge tank exit)	146 kPa
Intake charge composition	17.963 vol% O_2, 79.441 vol% N_2, 2.596 vol% CO_2 (20% simulated EGR)
Fuel	63.5 vol% 2,2,4,4,6,8,8 – heptamethylnonane, 36.5 vol% n-hexadecane
Injection pressure	1615 bar

Table 3. Injection timings and fuel mass injected.

	SOI Early injection timing (CAD aTDCc)	SOI Intermediate injection timing (CAD aTDCc)	Fuel mass (mg)
Pilot 1	-16.225	-12.225	2.2
Pilot 2	-4.1	-0.1	2.1
Main	5.7	9.7	38.3

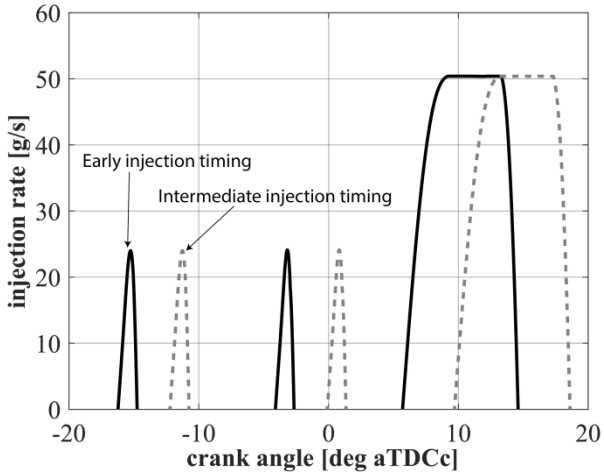

Figure 2. Injection profile of the early near-TDC and intermediate injection timings.

To analyze the effects of piston bowl geometry on vortex formation, two piston meshes are simulated in this study: the baseline stepped-lip (SL) piston, and the dimpled stepped-lip (DSL) piston. Their mesh topologies are shown in Figure 3. The dimples of the DSL piston are aligned with the spray axis of each of the eight nozzles.

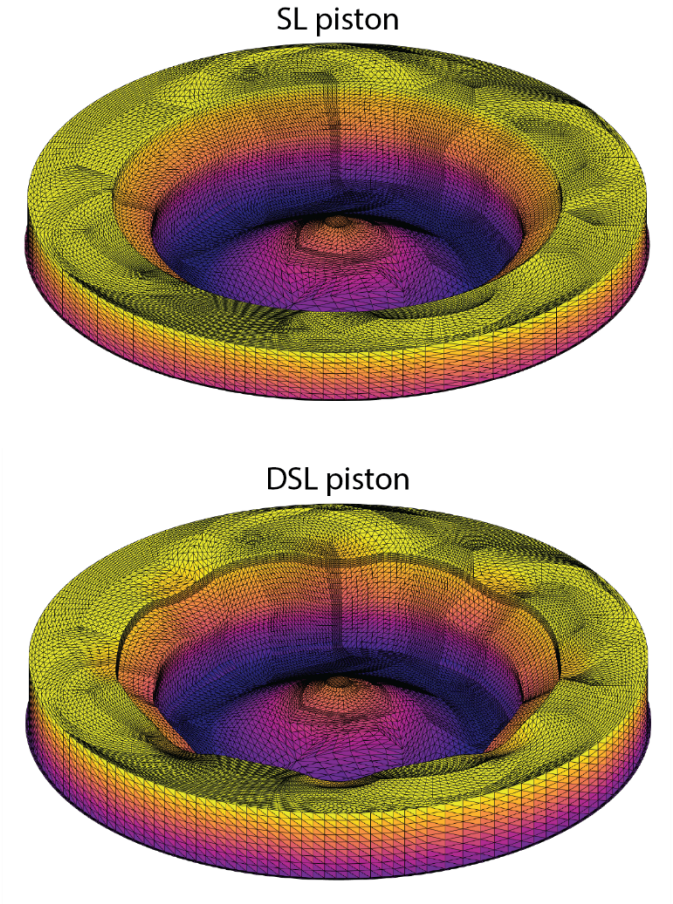

Figure 3. Mesh configurations of the SL and DSL pistons.

Geometry Variations

The DSL piston's dimple geometry is varied in a sensitivity study. The stepped-lip piston profile (z_{SL}) is defined in r-z coordinates by a connected series of lines and circular arcs as shown in Figure 4. Sweeping this profile 360° around the piston axis creates the baseline stepped-lip bowl geometry, which is shown as a dashed line. The DSL piston geometry is based on the same lines and arcs. To create the dimples, the three circular arcs and two linear profiles that define the step are shifted downward by a distance d that varies with azimuthal angle θ:

$$d = d_o\left(\frac{1 + \cos(\theta n_{holes})}{2}\right)^O \tag{1}$$

Here, d is dependent on the dimple depth d_o, and the azimuthal order O, which is the ratio of the dimple width to the azimuthal steepness. n_{holes} is the number of injector nozzle holes, which in this case is 8. Figure 4 indicates which segments are shifted vertically. The length of the short linear segment that connects the circular arcs defining the toroidal bowl and inner rim of the step region is adjusted to maintain continuity as the dimple depth changes. If the value of d is sufficiently large for a given value of θ, the linear segment is removed, and a non-linear solver is applied to ensure tangency of the two remaining circular arcs to one another. A sigmoid function describes the s-shaped curve connecting the final arc of the step to the outermost horizontal segment. In this work, this curve is defined by a logistic function:

$$z_{DSL,\,logistic} = \begin{cases} 0 & if\ d = 0 \\ \dfrac{d}{1 + \exp(-k(r - x_c))} & otherwise \end{cases} \tag{2}$$

The steepness of this curve is defined by the parameter k, and x_c determines the horizontal location of the midway point of the curve. $z_{DSL,\,logistic}$ is shifted and normalized to ensure continuity at its end points.

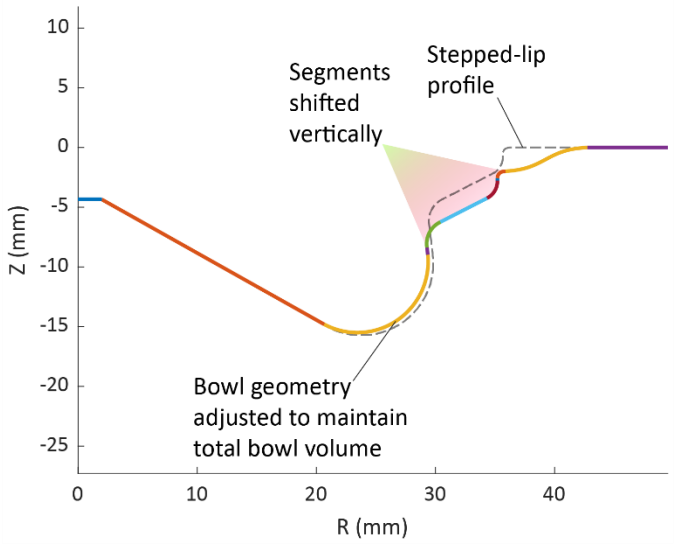

Figure 4. SL piston geometry is made of a connected series of lines and circular arcs (represented by different colors), which are swept 360° to create the SL piston. The DSL piston is based on these lines and circular arcs with segments shifted vertically downwards to create the dimples.

The DSL profiles are computed iteratively as follows:

1. The three-dimensional DSL geometry is created using the desired values of dimple depth d_o, azimuthal order O, dimple radial steepness k, and dimple radial extent x_c.
2. The bowl volume is computed from the surface-normal vectors using the divergence theorem.
3. Bowl dimensions are scaled by the cube root of the ratio of the baseline SL bowl volume to that computed in step 2 and the bowl is regenerated (see step 1).

These steps are repeated until convergence of the bowl volume to within 10 mm³ is achieved, typically within one or two iterations. This represents a maximum deviation in bowl volume of less than 0.03%.

The parameters that are varied in this study are d_o, k, o, and x_c. Each of these parameters are varied while the other three are kept constant, to isolate the effect of each parameter on spray-wall interactions and vortex formation. The effect of varying each parameter is shown in Figure 5. The baseline DSL bowl has a 2 mm dimple depth, radial steepness of 1, order of 2, and horizontal location of 3.5 mm.

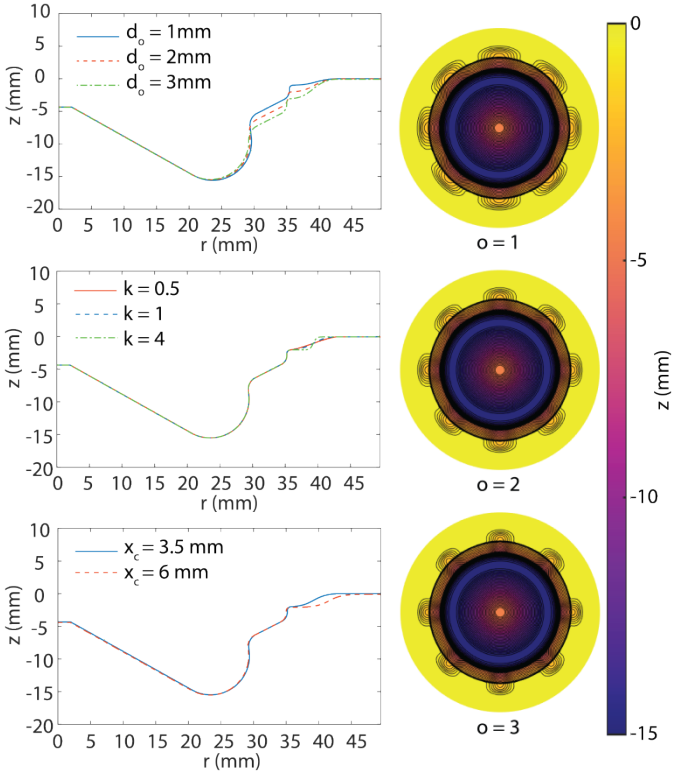

Figure 5. Effects of changing dimple depth d_o, radial steepness k, horizontal location x_c, and azimuthal order O on DSL piston geometry.

Experimental Setup

Engine experiments are carried out in the Sandia medium-duty diesel research engine as specified in Table 1. A schematic of the engine is shown in Figure 6. More information on the engine setup can be found in [37]. The engine is operated at part-load, as summarized in Table 4. A dual-pilot, single main injection strategy with constant dwell between each injection is used, and block-shifted by 2 crank angle degrees (CAD) to analyze effect of injection timing on engine efficiency and emissions. The main injection duration is adjusted to maintain a constant $IMEP_n$ for each injection timing, in contrast to the simulations where the main injection quantity is held constant for each injection timing. However, such adjustments were on the order of tens of microseconds which are not expected to have a significant effect on spray-wall interactions as described in the simulations. The injection energizing durations were determined using a hydraulic injection analyzer. Table 4 lists the start of energizing (SOE) time for each injection. The intake mass flow rate is kept constant, with constant intake compositions computed using a representative fuel flow rate to simulate a 20% EGR rate. Exhaust gases are diluted and cooled using nitrogen dilution before entering the exhaust surge tank.

Table 4. Engine operating part-load condition.

Intake temperature	44 °C
Coolant temperature	90 °C
Engine speed	1600 RPM
$IMEP_n$	8.55 bar ± 0.1 bar
Intake flow rate	14.9 g/s
Intake pressure (not controlled)	137 kPa
Simulated EGR	20%
Intake [O_2]	17.963 vol%
Intake [N_2]	79.441 vol%
Intake [CO_2]	2.596 vol%
Exhaust back pressure	146 kPa
Exhaust dilution flow rate	10 g/s nitrogen
Rail pressure	1615 bar
Injection strategy	2 pilots, 1 main
Injection sweep	Blockshift entire injection strategy by 2 CAD
SOE pilot 1	-18.6 CAD aTDCc to -8.6 CAD aTDCc
SOE pilot 2	-6.9 CAD aTDCc to 3.1 CAD aTDCc
SOE main	2.7 to 12.7 CAD aTDCc

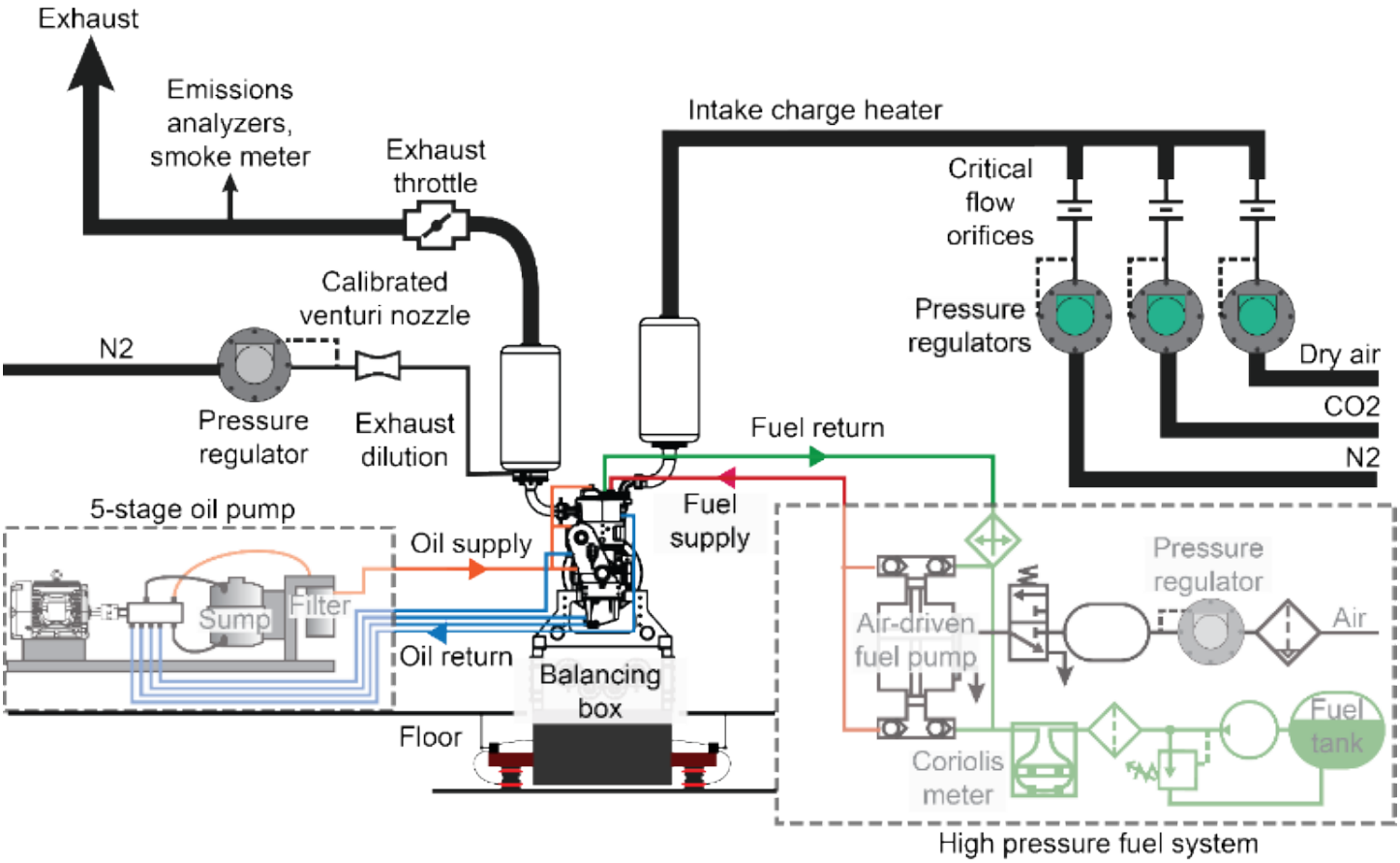

Figure 6. Experimental setup.

Cylinder pressure was measured with an AVL GH14P pressure transducer, mounted in a glow plug adaptor. Smoke was measured with AVL 415S smokemeter. CO, NOx, and unburned hydrocarbons were measured with California Analytical Instruments' 300 NDIR, 600-HCLD, and 600-series FID analyzers, respectively.

The engine experiments were performed to provide insights into the engine's efficiency and emissions characteristics to two different piston bowl geometries: the baseline stepped-lip piston bowl, and the baseline dimpled stepped-lip piston bowl (shown in Figure 3). Fuel is injected using a centrally mounted 8-hole piezo injector. The dimples in the DSL bowl are aligned to each of the eight spray plumes to within 5°. The two piston bowl geometries are shown in Figure 7. Thermodynamic estimation of the compression ratio using method as described in [38] suggests that the DSL piston is within 0.1 points of the baseline SL piston. The surface area of the DSL bowl is approximately 2.4% smaller than the SL bowl.

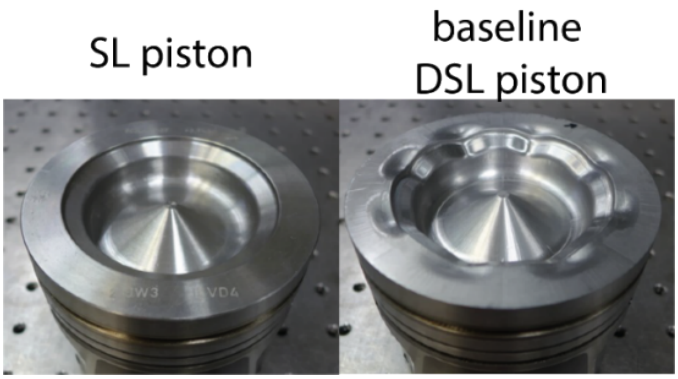

Figure 7. SL and DSL pistons used in engine experiments. The DSL piston has been machined in-house from a piston blank.

Thermodynamic Analyses

The cylinder pressure measurements, intake flow rate and compositions, fueling rates, and emissions measurements are used to perform heat release rate analysis. The rate of heat release is computed using the first law of thermodynamics:

$$\frac{dQ_{HR}}{d\theta} = \frac{\gamma}{\gamma-1}P\frac{dV}{d\theta} + \frac{1}{\gamma-1}V\frac{dP}{d\theta} + \frac{dQ_{wall}}{d\theta} \quad (3)$$

The cylinder pressure trace P is filtered using a low-pass filter with a 3-dB cutoff frequency of 3.5 kHz. Then, the heat-release rate is computed as a function of crank angle for each of approximately 260 cycles. The heat-release data shown here represents the ensemble average of these heat-release traces. V is the cylinder volume. γ is the ratio of specific heats, which is computed as a function of temperature and modeled mixture composition. The mixture composition comprises of the fresh intake charge with EGR components, and products of a complete, stoichiometric combustion computed with the mass fraction burned. Fuel liquid/vapor and incomplete combustion products are not considered in the calculation of γ.

The wall heat loss $\frac{dQ_{wall}}{d\theta}$ is given by

$$\frac{dQ_{wall}}{d\theta} = \frac{h_{Woschni}A}{N}(T_{cyl} - T_{wall}) \quad (4)$$

Here, A is the instantaneous combustion chamber surface area, T_{cyl} is the bulk gas temperature computed from ideal gas law, T_{wall} is the wall temperature, assumed to be 90 °C, and N is the engine speed in revolutions per second. $h_{Woschni}$ is the corrective heat transfer coefficient computed using the Woschni correlation [39-41]:

$$h_{Woschni} = C_m B^{-0.2} P^{0.8} T_{cyl}^{-0.546}\left[C_1 v_{piston} + C_2(P - P_{mot})\right]^{0.8} \quad (5)$$

B is the bore diameter, P is the combustion cylinder pressure, P_{mot} is the motored cylinder pressure computed similar to [40], and v_{piston} is the mean piston speed. The constant C_1 during the closed portion of the cycle is given by:

$$C_1 = 2.28 + 0.308\frac{\pi B R_s}{2S} \quad (6)$$

These values are taken from [39], with S being the stroke of the engine, R_s the swirl ratio assumed to be 1.7 [28]. C_m and C_2 are calibrated for each operating condition and injection timing according to Dernotte et al. [40]. First, C_m is calibrated using only the motored pressure traces until the integrated apparent heat release is equal to the integrated wall heat loss. Once C_m is obtained, C_2 is then adjusted using fired cylinder pressure traces until the average integrated heat release at exhaust valve opening, $Q_{HR,EVO}$, is equal to the amount of fuel energy released as heat:

$$Q_{HR,EVO} = Q_{fuel\,released} = m_{fuel}Q_{LHV}\eta_{comb} \quad (7)$$

m_{fuel} is the measured fuel mass per cycle, Q_{LHV} the lower heating value as described in Table 5. For this study, C_m is obtained for the SL and DSL piston separately, and C_2 is obtained for each injection timing. Note that using the same C_m and C_2 values for all experimental datasets reveals similar trends in the heat-release rate analysis.

Table 5. Certification diesel fuel properties.

Property	**Value**
Lower heating value (MJ/kg)	42.93
Density (kg/m^3)	0.8689
Cetane number	46

η_{comb} the combustion efficiency calculated using the exhaust emissions measurements:

$$\eta_{comb} = 1 - \frac{\dot{m}_{exhaust}(y_{UHC}Q_{LHV} + y_{CO}Q_{LHV,CO})}{\dot{m}_{fuel}Q_{LHV}} \quad (8)$$

Here, y_{UHC} and y_{CO} are the mass fractions of the unburnt hydrocarbons and CO, $Q_{LHV,CO}$ is the lower heating value of CO (10.10 MJ/kg), and $\dot{m}_{exhaust}$ and $\dot{m}_{fuel}$ are the mass flow rates of the exhaust and fuel.

The mass fraction burned (MFB) is equal to

$$MFB = \frac{Q_{HR}}{Q_{HR,EVO}} \quad (9)$$

Here, Q_{HR} is the cumulative heat release. The thermal efficiency is obtained from net indicated work W_i, boundary work over entire cycle, and fuel energy released:

$$\eta_{th} = \frac{W_i}{Q_{HR,EVO}} \tag{10}$$

The wall heat transfer is also normalized as:

$$Q_w^* = \frac{Q_w}{Q_{HR,EVO}} \tag{11}$$

The degree of constant volume combustion (dCVC) is obtained from the heat release trace and characterizes the degree to which the heat release rate represents ideal, constant volume combustion. Increasing dCVC generally means that the heat release is taking place earlier during the expansion stroke and more work can be extracted from the gas in the cylinder. The dCVC is calculated using

$$dCVC = \frac{1}{\eta_{Otto} Q_{HR,\,EVO}} \int \left(1 - \left(\frac{V_d + V_c}{V}\right)^{1-\gamma} \frac{dQ_{HR}}{d\theta}\right) d\theta \tag{12}$$

Here, V_c is the clearance volume, V_d the displacement volume, V the instantaneous volume, and η_{Otto} is the Otto cycle efficiency:

$$\eta_{Otto} = 1 - r_c^{1-\gamma} \tag{13}$$

Where r_c is the compression ratio and γ the specific heat ratio equal to 1.33.

Results

Simulation Results

DSL Baseline vs SL pistons

The spray and flow development on a vertical cut-plane aligned with one of the spray axes is depicted in Figure 8. The SL piston with early injection timing (left column), SL piston with intermediate injection timing (center column), and the DSL baseline piston with early injection timing (right column) are shown. The cutting plane is colored by the fuel-air equivalence ratio, Φ. The black contour represents the stoichiometric (Φ=1) isosurface. Note that the spray-wall interactions and turbulent flow development vary from spray to spray due to local features on the cylinder head, i.e. valve recesses [36], mesh-dependent effects, and flow asymmetry, but all important features discussed here are predicted to occur in each of the sprays. Therefore, only a single vertical cutting plane is shown.

At 6 CAD after the start of the main injection (aSOImain), the spray has already impinged on the lower bowl rim. This impinging spray separates at the rim into two portions, a lower portion that enters the toroidal part of the bowl, and an upper portion that deflects upwards along the vertical step, towards the cylinder head, and into the squish region. At 8 CAD aSOImain, Figure 8 shows that due to lower charge density and changes in piston position, fuel splitting, and momentum distribution, more of the fuel enters the squish region in the SL piston at the intermediate injection timing than the early injection timing. In the DSL simulation, the upper portion of the spray is deflected upwards towards the head surface by the step. Since the step region of the DSL bowl is lower than in the SL piston at the early injection timing, this deflection is not as strong in the DSL bowl.

At 10 CAD aSOImain, the fuel has begun to impinge on the head surface. Part of the spray is driven inwards towards the bowl above the step, while part of the flow is driven outwards into the squish region. The inwards and outwards flows are stronger in the SL piston when injection timing is retarded. The outward flow is also directed downwards towards the piston surface in the intermediate injection timing simulation. In the DSL piston, the outward flow is as strong as that of the SL piston with intermediate injection timing. The inward flow in the DSL piston is stronger than the SL piston with early injection timing.

At 12 CAD aSOImain, the outward flow is directed towards the piston surface in the SL and DSL pistons with early injection timing simulation. At the intermediate injection timing, the piston has moved further downwards, and the outward flow is directed more perpendicular towards the piston surface. By 14 CAD aSOImain, the outward flow starts to form a clockwise vortex in the squish region. They are predicted to be weaker in the SL piston with early injection timing, and stronger when injection timing is retarded, as evident by the larger recirculation zone. In the DSL piston, the space in the squish region that is available in the SL piston at intermediate injection timing is recovered by the added dimple at advanced injection timing. This allows more of the spray and its momentum to enter the squish region to form the clockwise recirculation zone. These dimples have been predicted to promote vortex formation in a small-bore diesel engine in a previous study [3].

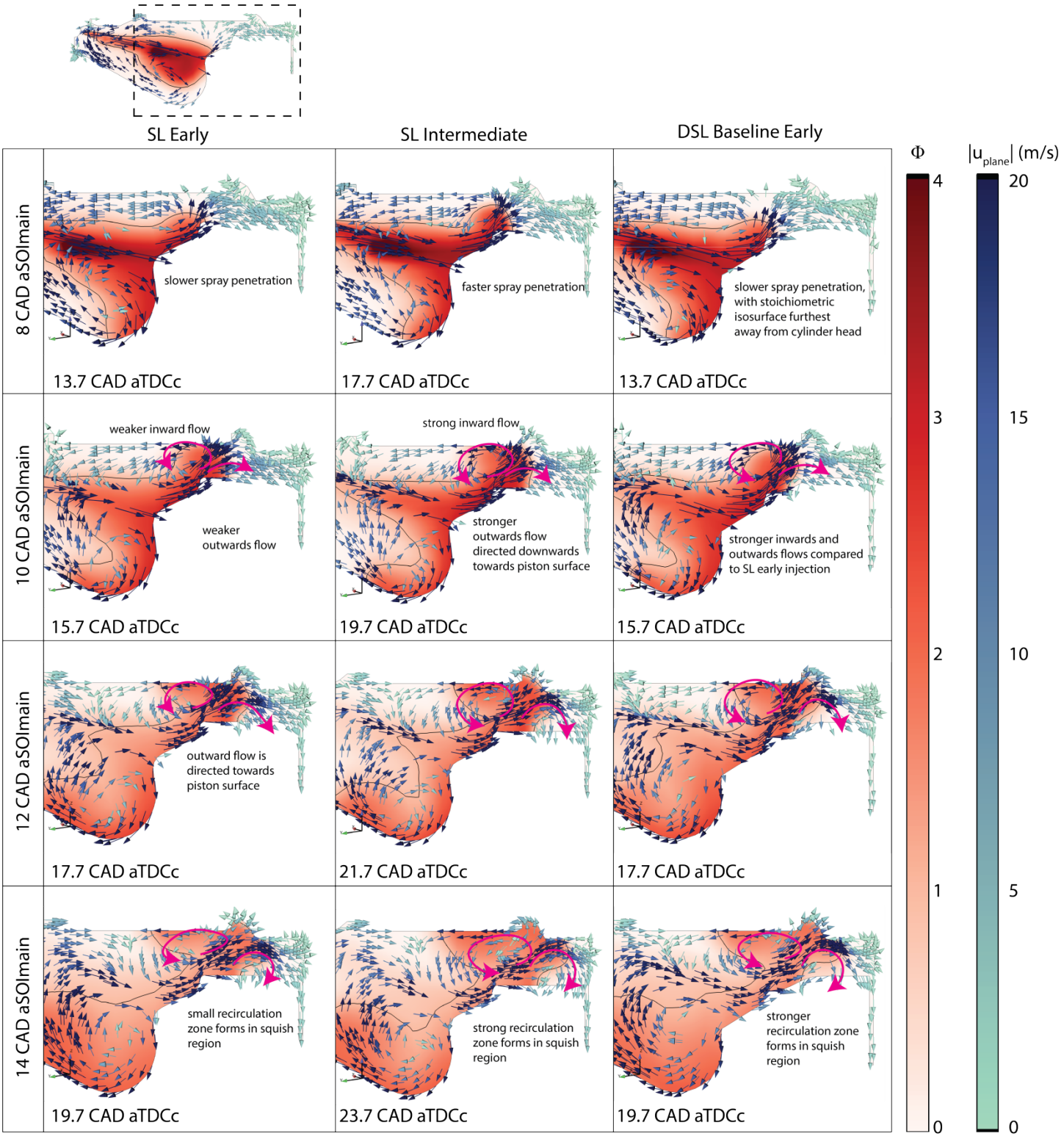

Figure 8. Equivalence ratio and in-plane velocity on a vertical cutting plane (through nozzle 6 axis). Black line is the stoichiometric isosurface. Magenta-colored large vectors are added to show the recirculation zones. As can be seen, two recirculation zones form in the squish region: a counter-clockwise vortex above the step near the cylinder head, and a clockwise vortex in the squish region. The squish-region clockwise vortex appears stronger in the SL intermediate injection timing and DSL baseline early injection timing.

To understand the mechanisms of squish-region vortex formation, the radial momentum equation is analyzed in detail. This is done by analyzing each term of the radial Navier-Stokes equation, normalized by the local velocity:

$$\frac{1}{|\vec{u}|}\frac{\partial u}{\partial t} = -\frac{1}{\rho|\vec{u}|}\frac{\partial p}{\partial r} - \frac{1}{|\vec{u}|}\left(u_r\frac{\partial u_r}{\partial r} + \frac{u_\theta}{r}\frac{\partial u_r}{\partial \theta} + u_z\frac{\partial u}{\partial z} - \frac{u_\theta^2}{r}\right) + \frac{\mu}{\rho|\vec{u}|}\left(\frac{\partial}{\partial r}\left(\frac{1}{r}\frac{\partial}{\partial r}(ru_r)\right) + \frac{1}{r^2}\frac{\partial^2 u_r}{\partial \theta^2} + \frac{\partial^2 u_r}{\partial z^2} - \frac{2}{r^2}\frac{\partial u_\theta}{\partial \theta}\right) + \frac{1}{\rho|\vec{u}|}\frac{\partial \tau_{rr}}{\partial r} \quad (14)$$

The previous study in a small-bore engine shows that only the radial pressure gradient $\frac{-1}{\rho|\vec{u}|}\frac{\partial p}{\partial r}$ and the vertical convection of radial momentum $\frac{1}{|\vec{u}|}u_z\frac{\partial u}{\partial z}$ contribute in a significant way to the radial acceleration $\frac{1}{|\vec{u}|}\frac{\partial u}{\partial t}$ in the squish region entrance, and that all other terms have negligible effects in that location [3, 19]. The simulations in this study show similar results, therefore, only the radial acceleration, radial pressure gradient, and the vertical convection terms will be shown.

Figure 9 shows the radial acceleration on the vertical cutting plane at 10 CAD aSOImain, along with inserts of the radial pressure gradient and the vertical convection terms showing their contributions to the radial acceleration in the entrance to the squish region. Each term is normalized by the local velocity magnitude and has units of 1/CAD. The inward acceleration near the cylinder head, as indicated by the blue region, is due to negative (adverse) pressure gradients around the head of the spray. This area of adverse pressure gradient forms due to increasing pressure in the radial direction near the cylinder head surface as the spray enters and stagnates in the squish region, as described in [3, 19]. A region of lower adverse pressure gradient is found along the center of the spray. Near the piston surface, the adverse pressure gradient increases again. Coinciding with the adverse pressure gradient near the cylinder head is a region of strong positive vertical convection of radial momentum towards the cylinder head surface. Near the piston surface, the radial momentum is transported downwards resulting in negative values of the vertical convection term. The vertical convection term competes with the radial pressure term, resulting in a positive outward acceleration at the center of the spray, and negative, inward acceleration near the piston and head surfaces.

Details of the radial terms show the reason for stronger radial acceleration in the center of the spray in the SL piston at intermediate injection timing: there exists a larger gap between the two adverse pressure gradient areas near the surfaces of the head and piston due to the lower piston position. The location of the pressure gradient inversion to positive values is located at the bowl rim regardless of dimple depth. The area of positive vertical convection term is also larger. This results in a larger area of stronger, positive radial acceleration of the fuel spray into the squish region. The SL piston with early injection timing shows a smaller gap between the two adverse pressure gradients near the surfaces, and a smaller region of positive vertical convection. This results in a less beneficial alignment between the two terms, and a smaller region of positive acceleration into the squish region. In contrast, the recovery of the space in the squish region in the DSL piston at early injection timing allows for a larger gap between the negative radial pressure gradients, and the distribution of radial pressure gradient is more angled following the curvature of the dimple. The area of positive vertical convection term is also larger. This leads to a larger area of positive radial acceleration compared to the SL piston, even at advanced injection timing. At the piston surface, a small region of negative radial acceleration exists, which indicates that fuel spray is being driven inwards, providing the mechanism for the clockwise rotation in the squish region. This negative radial acceleration term is larger in the DSL bowl than in the SL piston at either injection timings due to a more negative radial pressure gradient zone in near the dimple surface. The spatial distribution of radial acceleration, radial pressure gradient, and vertical convection of radial momentum is very similar to results from a small-bore diesel engine, where the vertical misalignment between positive vertical convection term and negative radial pressure gradients better improves the outward acceleration of the spray [3]. However, the entire front of the spray encounters a highly negative pressure gradient zone, which causes a competing inward acceleration at the front of the spray.

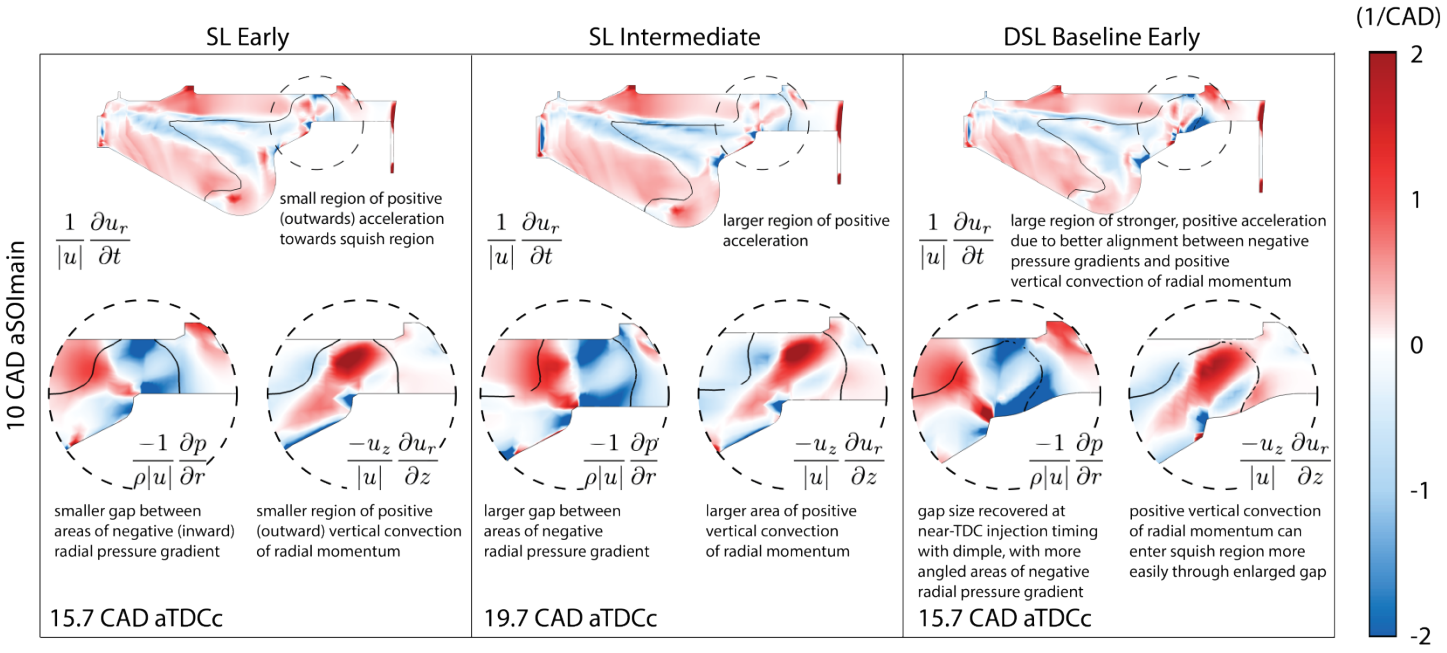

Figure 9. Radial acceleration, radial pressure gradient, and vertical convection of radial momentum, normalized by local velocity, on a vertical cut-plane at 10 CAD aSOImain, showing better misalignment between radial pressure gradient and vertical convection of radial momentum with the DSL piston, leading to more radial acceleration towards the squish region in the DSL piston despite near-TDC injection timing. Blue colors indicate inward acceleration towards the center of the combustion chamber, red colors indicate outward acceleration towards the liner.

In addition to the radial acceleration terms, the toroidal vorticity (normal to the vertical plane) can be used to show how rotational flow structures resulting from the fuel injection and spray-wall interactions are formed. The normalized toroidal vorticity is calculated using:

$$\omega_\theta = \frac{\left(\frac{\partial u_z}{\partial y} - \frac{\partial u_y}{\partial z}\right)sin\theta - \left(\frac{\partial u_x}{\partial z} - \frac{\partial u_z}{\partial x}\right)cos\theta}{M} \tag{15}$$

M is the engine speed in revolutions per CAD. Positive ω_θ is associated with counter-clockwise rotation and negative ω_θ with clockwise rotation.

Note that vorticity can exist without rotational flow as it is also generated in shearing flow. Therefore, the existence of vorticity does not necessarily indicate the existence of a vortex. To visualize vortex cores, the Q-criteria can be used [42]. The Q-criterion is calculated using:

$$Q = \frac{1}{2}\left(|\Omega|^2 - |S|^2\right) > 0 \tag{16}$$

It defines a vortex as a region where the magnitude of the vorticity tensor Ω dominates the magnitude of the strain rate tensor S. In this study, a threshold of $Q = 5 \times 10^6 \frac{1}{s^2}$ is used to visualize the vortices generated by the spray-wall interactions. This threshold value was chosen to best visualize the squish-region vortices and minimize structures identified by the Q-criteria near the surfaces. Higher threshold values cause such vortices to disappear. As such, this vortex-identification method is sensitive to the chosen threshold value and there is no consensus as to what threshold value to use [43]. However, comparable values may be found in the literature for the analysis of engine flows and range from 1×10^6 to $2 \times 10^7 \frac{1}{s^2}$ [44, 45].

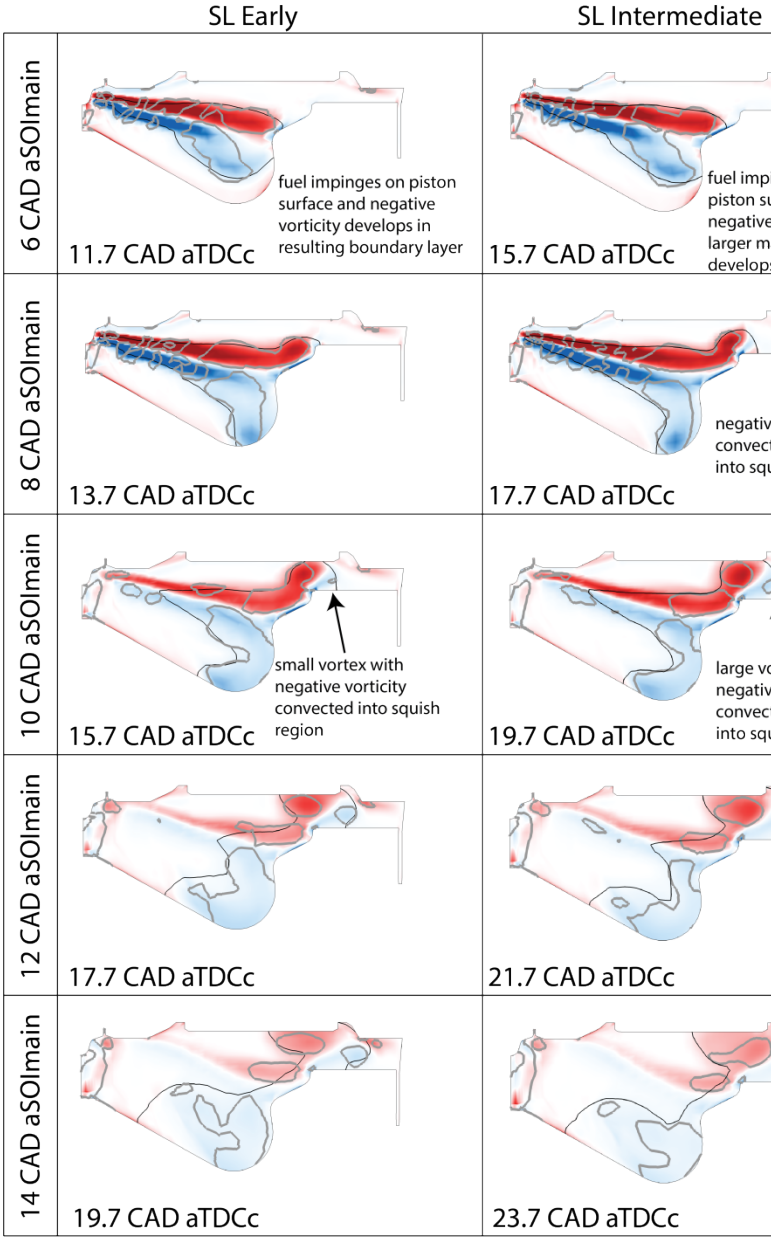

Figure 10 shows a vertical cut-plane of the vorticity, with the black outline indicating the location of the stoichiometric isosurface, and the thicker grey outlines represent the extents of the toroidal vortices as identified by the Q-criterion threshold. The blue colors indicate negative, clockwise vorticity, and red colors indicate positive, counter-clockwise vorticity. By using both the vorticity and Q-criterion, it can be seen that as the spray impinges on the bowl rim at 6 CAD aSOImain, negative vorticity is generated in the resulting boundary layer. The region of negative vorticity is larger in the intermediate injection timing of the SL piston, as the fuel spray impinges on a larger surface near the bowl rim. The vorticity is then transported upwards and outwards into the squish region, contributing to the formation of the clockwise vortex. This vortex is just forming at 8 CAD aSOImain in the SL piston with early injection

timing, while it is larger as injection timing is retarded. In the DSL bowl, a similar-sized vortex as that of the SL intermediate injection timing has also formed near the dimple surface. This vortex contains negative vorticity of a larger magnitude compared to the vortices found in the SL piston at either injection timing. At 10 CAD aSOImain, as the vortex develops further, it increases in size and is largest in the DSL piston. At 12 CAD aSOImain, the vortex remains larger in the DSL piston than in the SL piston at either injection timing. This is likely due to the larger positive radial acceleration in the center of the fuel spray in the DSL bowl, transporting more of the more negative vorticity into the squish region. The larger negative radial acceleration at the bottom of the spray helps to create a stronger recirculating flow region and therefore a stronger and larger vortex.

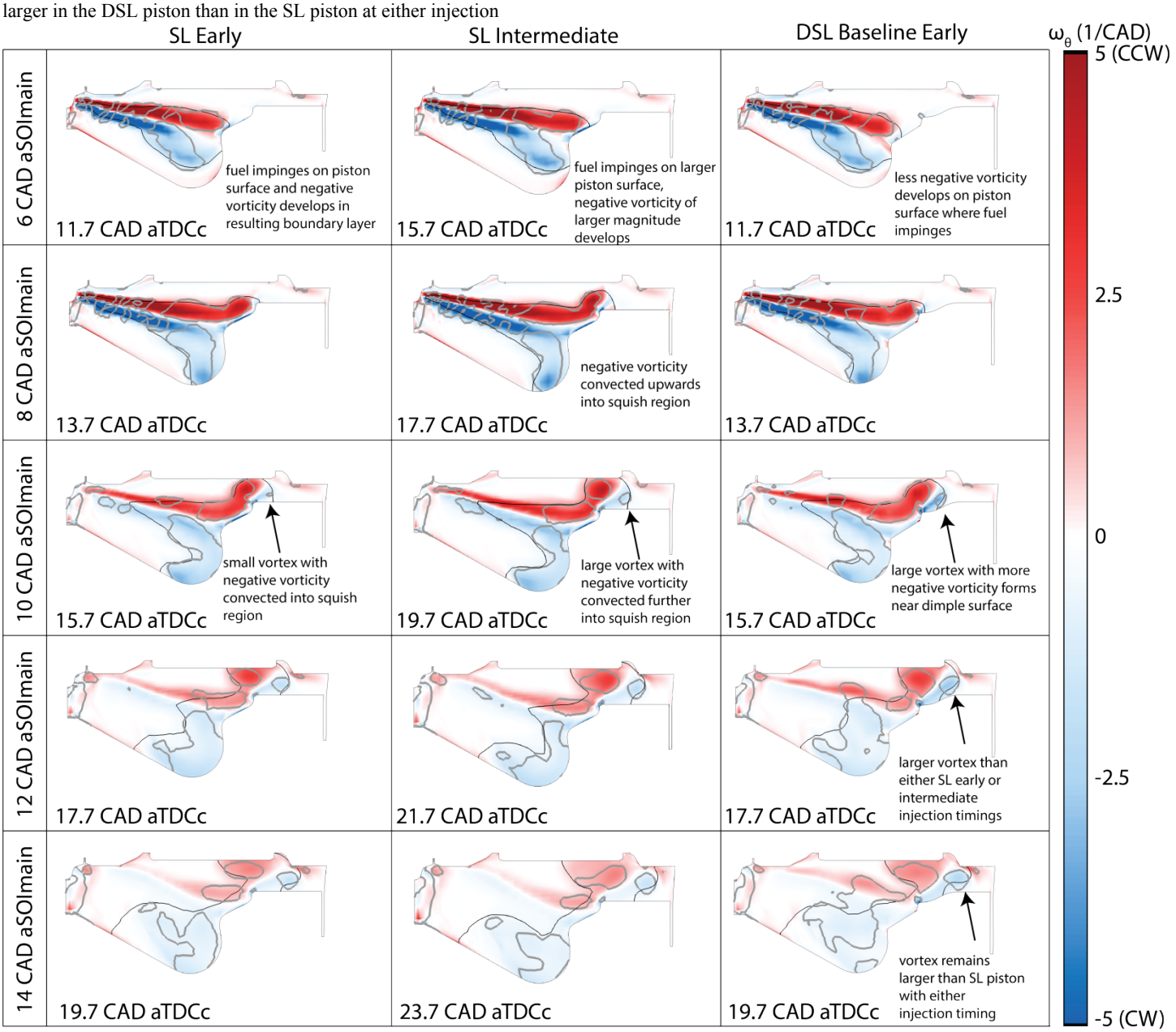

Figure 10. Toroidal vorticity on vertical cut-plane. Black line is the stoichiometric isosurface. Grey, thicker outlines are the vortices identified by Q-criteria with a threshold value of 5×10^6 1/s^2. Clockwise vortices with negative vorticity are found in the squish region. The formation of these vortices is stronger in the DSL piston, despite earlier injection timings.

Sensitivity Study Results

In order to quantify the vortex enhancement due to dimple geometry variations, the toroidal rotational energy and size of the squish-region vortices are calculated. The rotational energy is defined as

$$E_{rot} = \frac{1}{2}\sum I_i\omega_i^2 = \frac{1}{2}\sum \frac{m_i((z_i - z_c)u_{r,i} - (r_i - r_c)u_{z,i})^2}{(z_i - z_c)^2 + (r_i - r_c)^2} \quad (17)$$

Here, subscript i represents each cell inside the Q-isosurface, I_i is the moment of inertia, ω_i the angular velocity, m_i the mass, $u_{r,i}$ and $u_{z,i}$ the velocity components in the radial and z-directions, r_i and z_i are the radial and z position, and r_c and z_c the rotation center of the vortex core, defined as the position with maximum Q value. The CFD data is first filtered to remove cells located outside the vortices, cells with positive vorticity, and cells not in the squish region ($Q < 5e6\ 1/s^2$, $\omega_\theta > 0\ 1/CAD$, and $r_i < 0.035\ m$). The rotational energy is obtained over the filtered cells i on each azimuthal plane θ from $1°$ to $360°$ in $1°$ increments. Finally, the total rotational energy is summed over all azimuthal planes. In addition, the size of the vortices is captured by the total volume of the filtered cells over all azimuthal planes.

Figure 11 shows the total rotational energy and volume of the squish-region vortices as a function of CAD of the SL piston with early and intermediate injection timings, and the DSL pistons in the sensitivity study with early injection timing. The SL piston with early injection timing has the lowest peak rotational energy and smallest total volume overall. By retarding the injection timing, the peak rotational energy increased slightly with larger total volume. This reflects what is seen in

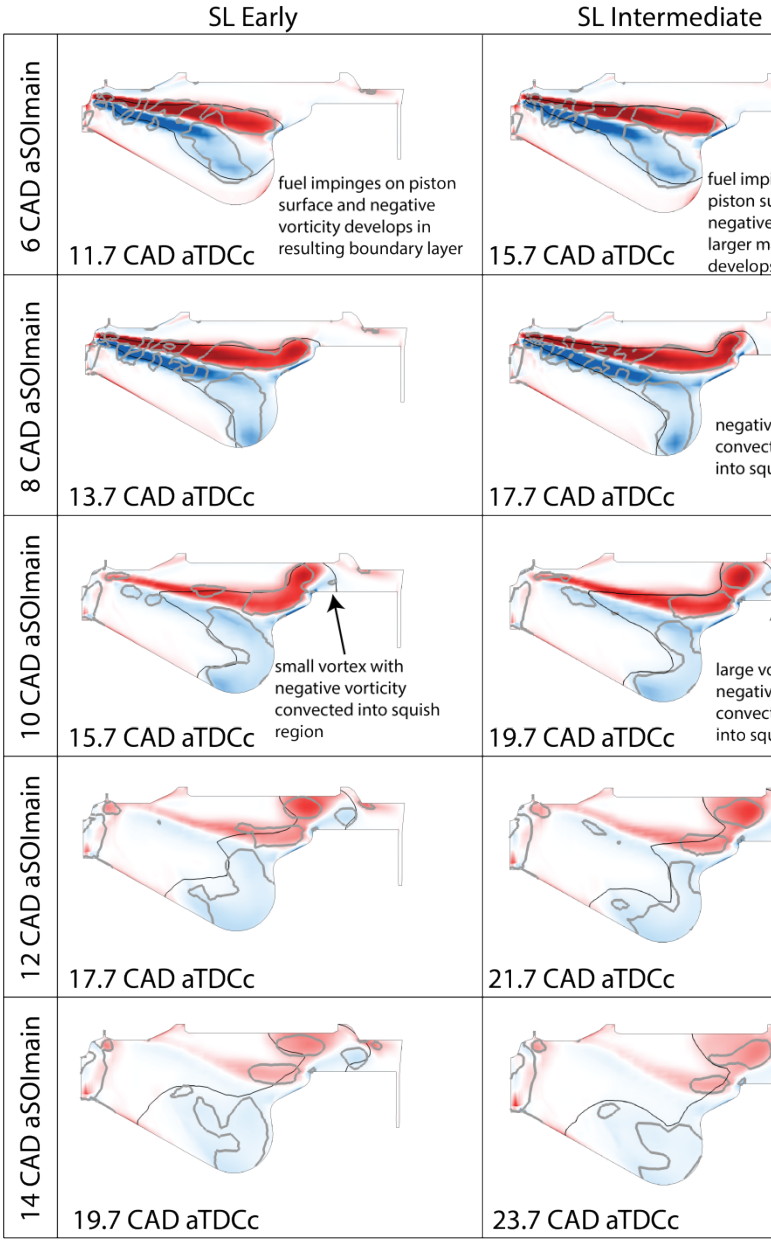

Figure 10: *the squish-region vortex is larger for the SL intermediate injection timing, and likely more energetic due to it containing more negative vorticity compared to the SL early injection timing. By using a DSL piston, even larger peak rotational energy and larger-sized vortices are produced despite the early injection timing. This was*

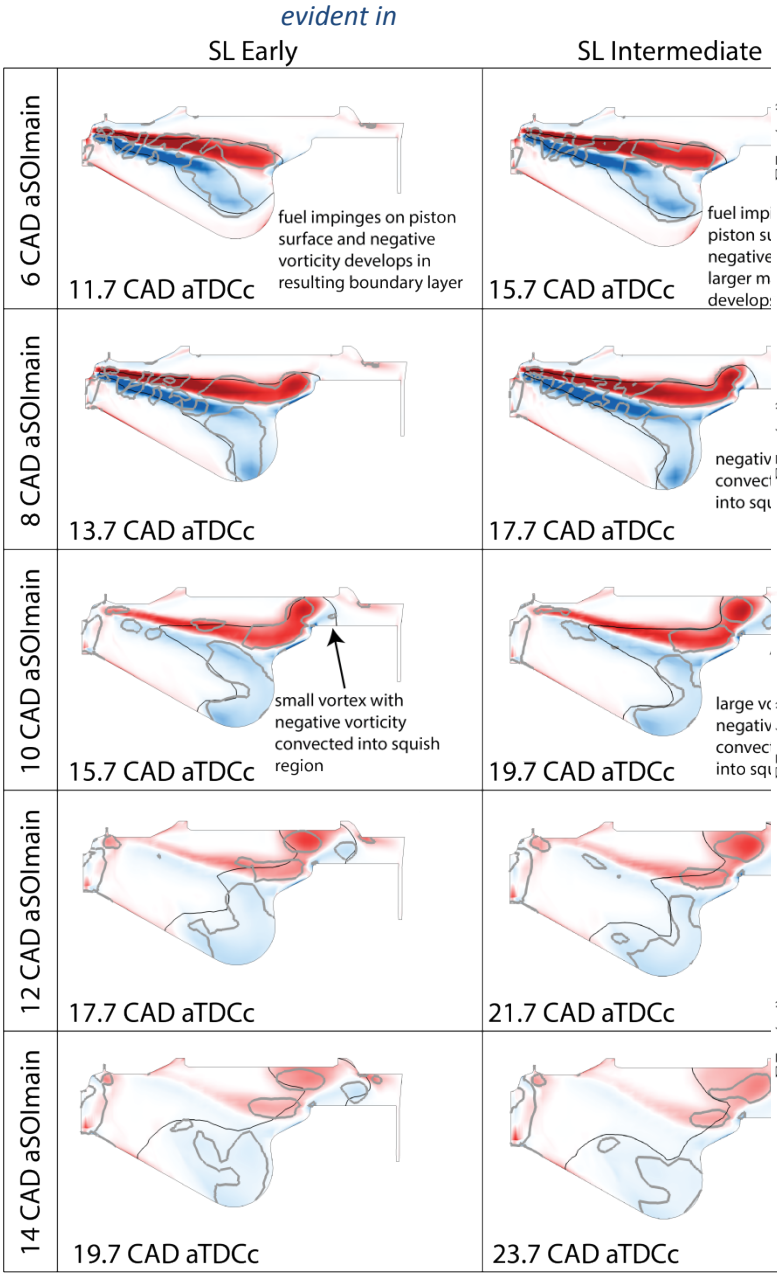

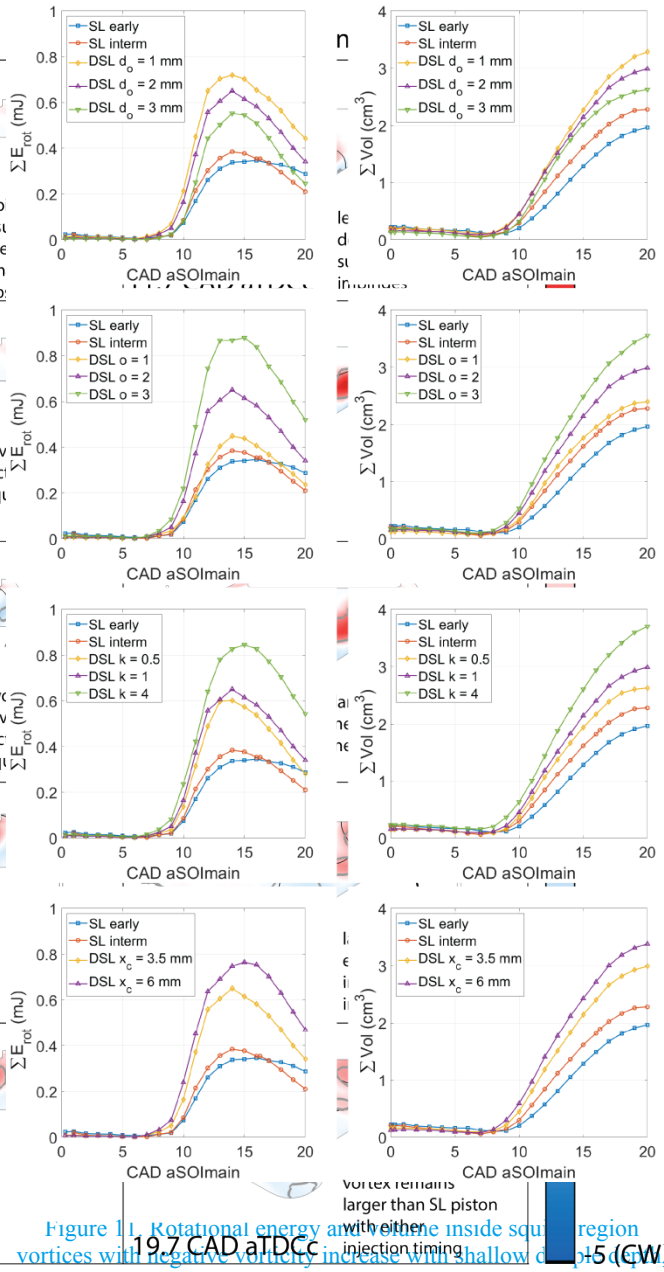

Figure 11. Rotational energy and volume inside squish region vortices with negative vorticity increase with shallow dimple depth, with sharper dimple features, i.e. increased azimuthal order, increased radial steepness, and increased horizontal location of the dimples.

Figure 10, as the simulation predicts larger vortices with even more negative vorticity in the DSL baseline piston. The sensitivity study shows that to increase rotational energy, the DSL geometry should have shallow dimple depths, but sharper geometric features, i.e. large azimuthal order o, increased radial steepness k, and larger radial extent x_c of the dimples.

Guided by the sensitivity study, an improved DSL bowl is generated which has the smallest dimple depth of 1 mm, the largest azimuthal order of 3, the highest radial steepness of 4, and the largest horizontal location of 6 mm. The improved DSL piston side and top profiles are shown in Figure 12, alongside the SL piston and the baseline DSL piston. The dimple in the improved bowl has a much flatter dimple with steeper radial and azimuthal curvatures, resembling a double stepped-lip piston [22, 23].

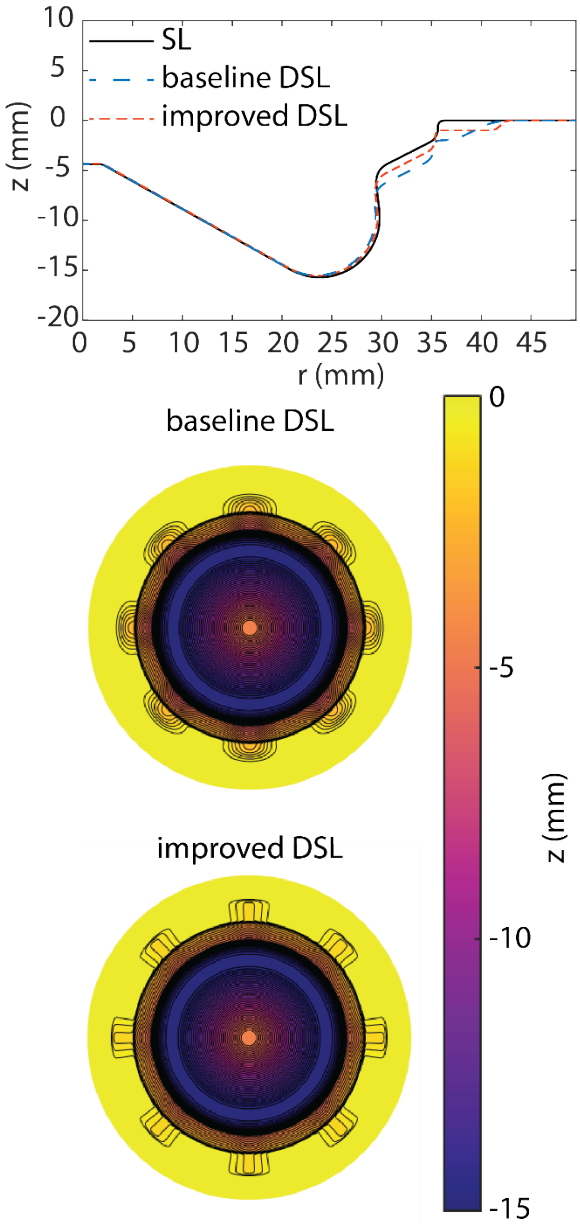

Figure 12. Baseline and improved DSL piston side profile and top view. The SL piston side profile is added as reference.

Figure 13 shows the radial acceleration, radial pressure gradient, and vertical convection of radial momentum terms of the SL piston with intermediate injection timing, and the baseline and improved DSL baseline pistons with early injection timing. The area of positive outward radial acceleration of the improved DSL bowl is larger compared to the baseline DSL and the SL pistons, and connected to the region of positive radial acceleration downstream of the head of the spray. The shape of the dimples in the improved bowl helps to reduce the adverse pressure gradient in the center of the spray. This allows for more of the positive vertical convection term to contribute to the positive radial acceleration term.

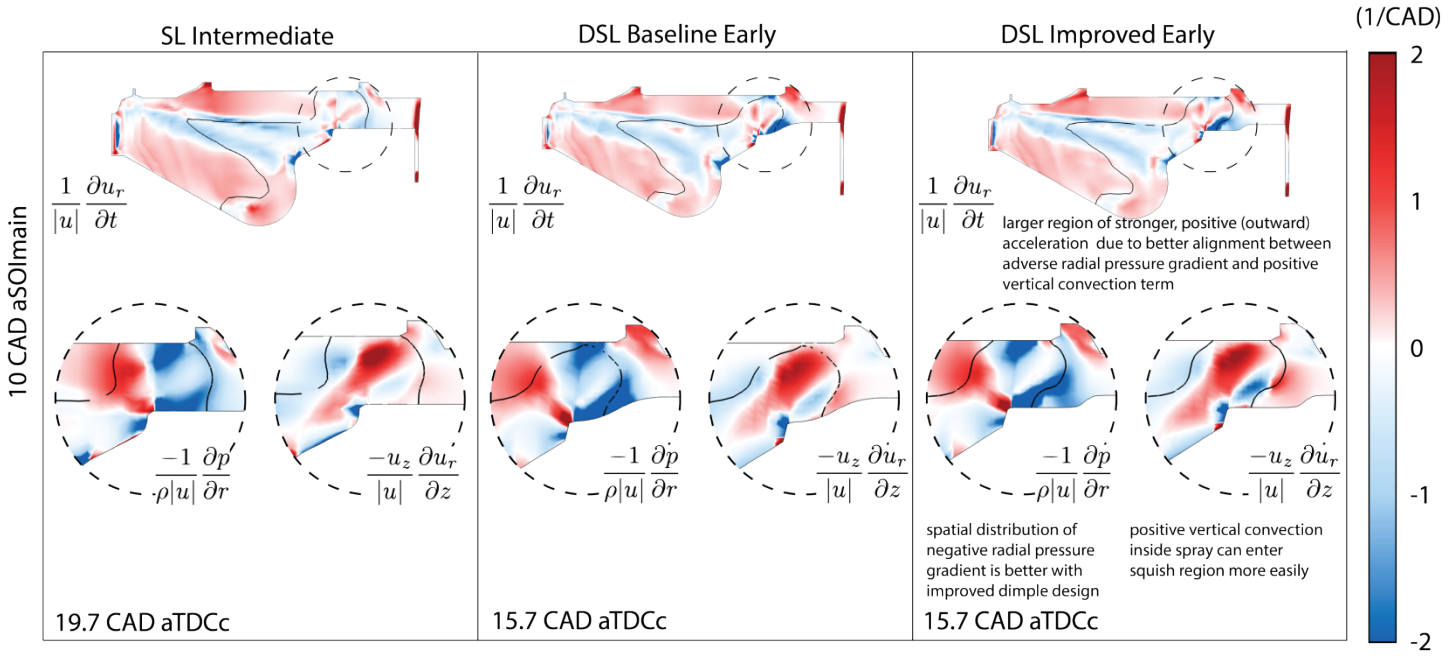

Figure 13. Radial acceleration, radial pressure gradient, and vertical convection of radial momentum, normalized by local velocity, on a vertical cut-plane at 10 CAD aSOImain. The DSL improved bowl has larger region of stronger, positive (outward) radial acceleration towards the squish region compared to either the DSL baseline bowl with early injection timing, or the SL bowl with intermediate injection timing. Blue colors indicate inward acceleration towards the center of the combustion chamber, red colors indicate outward acceleration towards the liner.

The toroidal vorticity is shown in

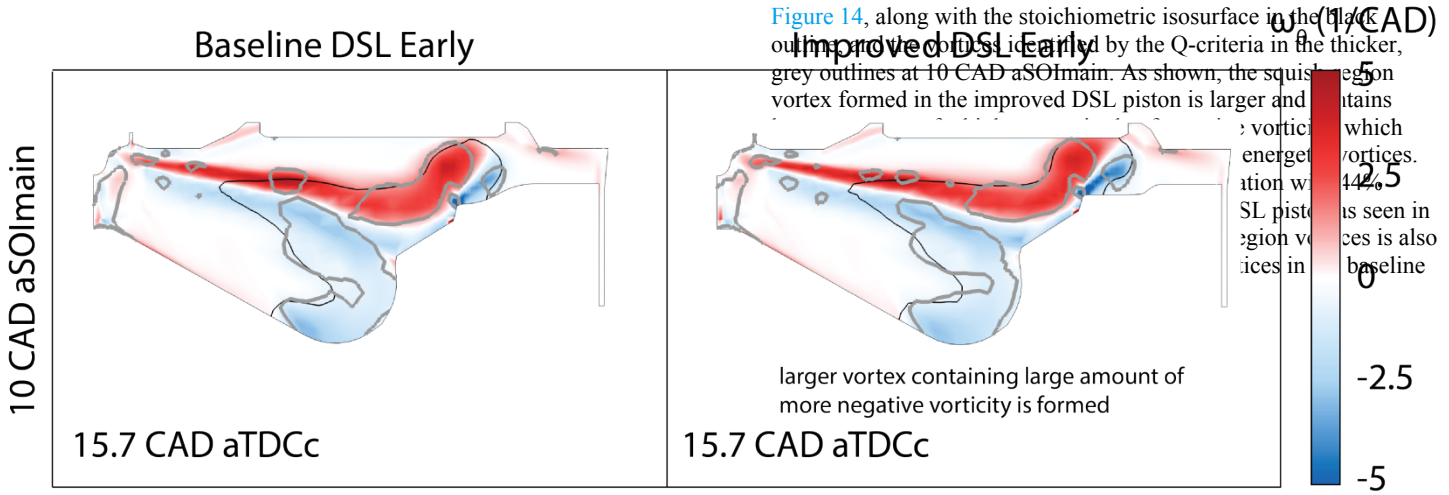

Figure 14, along with the stoichiometric isosurface in the black outline and the contours identified by the Q-criteria in the thicker, grey outlines at 10 CAD aSOImain. As shown, the squish region vortex formed in the improved DSL piston is larger and contains vorticity which energetic vortices. ation with 44% SL piston as seen in region vortices is also ices in baseline

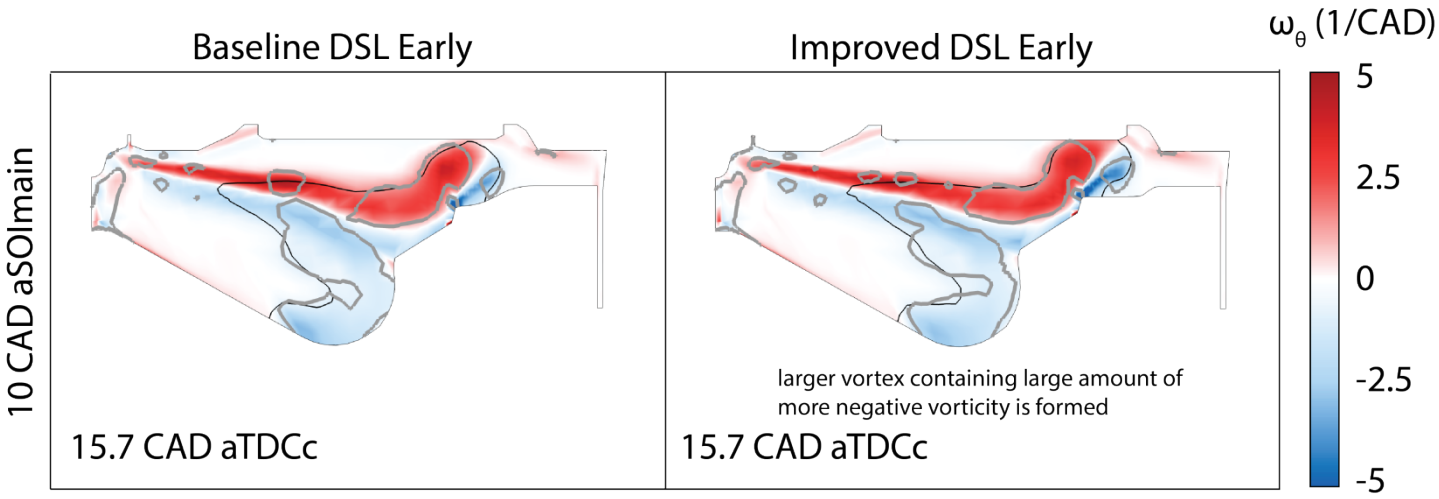

Figure 14. Toroidal vorticity on vertical cut-plane. Black line is the stoichiometric isosurface. Grey, thicker outlines are the vortices identified by Q-criteria with a threshold value of 5×10^6 1/s^2. Much larger and more energetic squish-region vortex is predicted to form in the improved DSL piston at early injection timing.

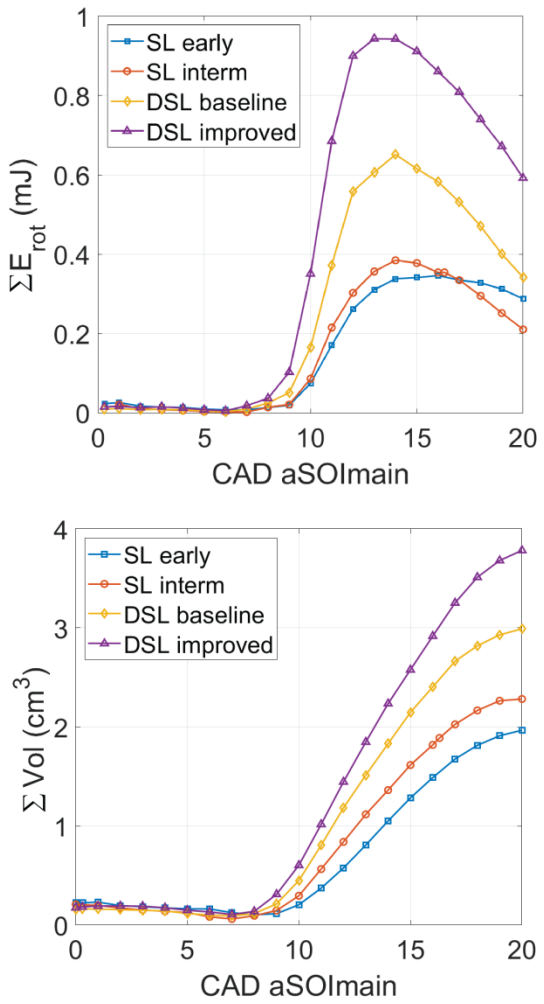

Figure 15. Improved DSL piston produces larger, more energetic squish region vortices than the baseline DSL design.

Experimental Results

The heat-release rate vs MFB are shown in the top figure in Figure 16 for the SL and DSL pistons with near-TDC injection timing at 2.7 CAD aTDCc. For both pistons, the peak heat release occurs before the crank angle where 50% of the heat is released (CA50). The heat release is enhanced by using the DSL piston at this injection timing. The bottom figure shows the heat-release rate as a function of crank angle after SOEmain (CA aSOEmain) for the near-TDC injection timing. The heat release of the pilot injections is lower in the DSL piston, while that of the main injection is higher than the SL piston. The higher heat-release rate during the main injection supports the CFD-predicted hypothesis that more energetic squish-region vortices promote faster mixing-controlled heat release.

Figure 17 shows the burn duration $CA_{50\text{-}90}$ of the SL and baseline DSL pistons as a function of injection timing. With main injection timings between 2.7 and 8.7 CAD aTDCc, the SL piston shows a monotonic decrease in $CA_{50\text{-}90}$ to a minimum of about 29.4 CAD, with about the same burn duration for main injection timing at 10.7 CAD aTDCc. Retarding the injection timing further leads to an increase in $CA_{50\text{-}90}$. In contrast, the $CA_{50\text{-}90}$ of the baseline DSL piston decreases between injection timings of 2.7 to 6.7 CAD aTDCc and are shorter than the $CA_{50\text{-}90}$ of the SL piston. After 6.7 CAD aTDCc, the $CA_{50\text{-}90}$ of the baseline DSL bowl increases. At near-TDC injection timing of 2.7 CAD aTDCc, the $CA_{50\text{-}90}$ of the baseline DSL piston is almost 4 CAD shorter than the SL piston due to faster mixing-controlled heat release.

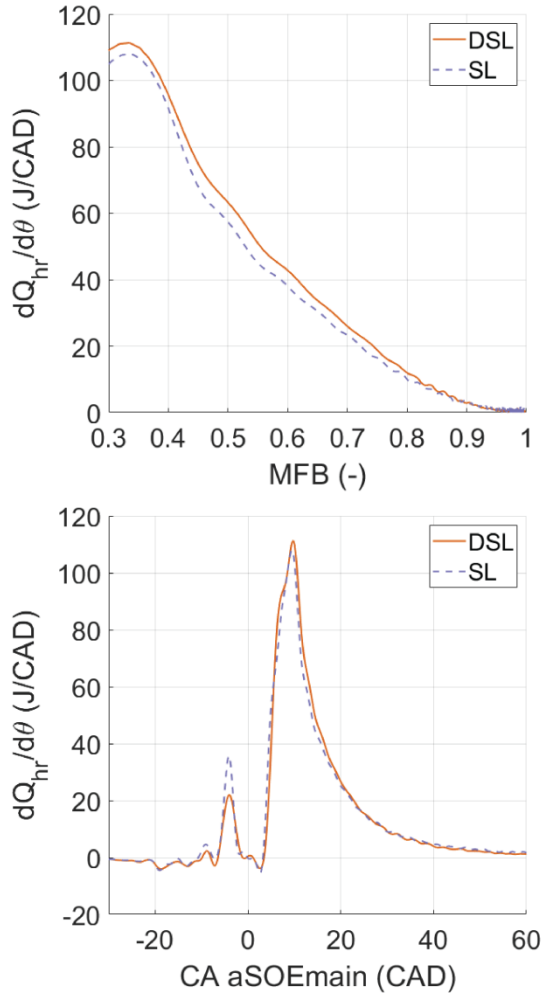

Figure 16. Top: Heat-release rate vs MFB for the near-TDC SOEmain of 2.7 CAD aTDCc showing faster mixing-controlled heat release with the DSL piston compared to the SL piston. Bottom: Heat-release rate vs CA aSOEmain for the near-TDC SOEmain of 2.7 CAD aTDCc.

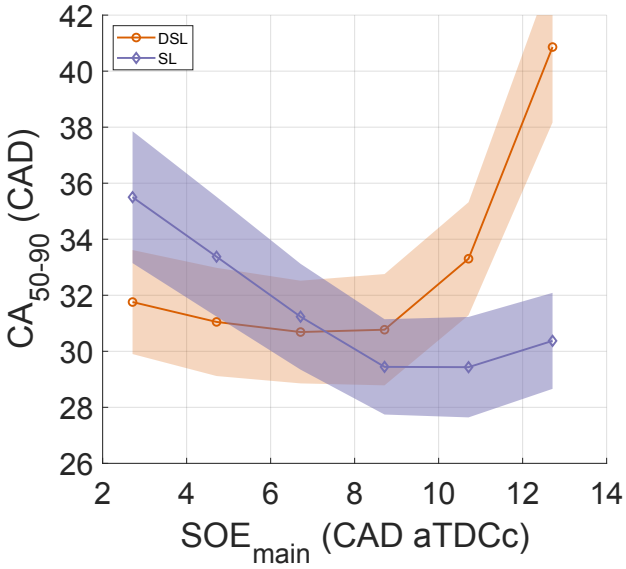

Figure 17. $CA_{50\text{-}90}$ vs SOE_{main}. The scatter band represents ±1σ of the more than 250 fired cycles, while each data point represents the ensemble average of these cycles. T-tests reveal that these results are statistically significant.

Thermal efficiency, normalized wall heat loss, and dCVC as a function of main injection timing are shown in Figure 18. The thermal efficiency gains and dCVC increases appear to be closely correlated. This correlation was established in a previous study on the engine performance using a conventional re-entrant bowl and a SL bowl, where they found that thermal efficiency gains with the SL piston were entirely attributed to higher dCVC values [4]. At near-TDC injection timing of 2.7 CAD aTDCc, the DSL piston is able to achieve a 1.4% relative gain in thermal efficiency compared to the SL piston. As injection timing is retarded, thermal efficiencies decrease with both piston geometries. After a main injection timing of 8.7 CAD aTDCc, the thermal efficiency gains with the DSL piston are lost. The dCVC is larger at the near-TDC injection timing for the DSL piston, but as injection timing is retarded, the dCVC of the DSL piston decreases below the values of the SL piston. At 2.7 CAD aTDCc injection timing, the calculated wall heat loss is about 2.3% smaller with the DSL piston, which is consistent with the 2.4% reduction in piston surface area. As injection timing is retarded, the wall heat loss decreases in both pistons, with lower heat loss persisting with the DSL piston. At 12.7 CAD aTDCc injection timing, however, the wall heat loss in the DSL piston increased by 0.3%.

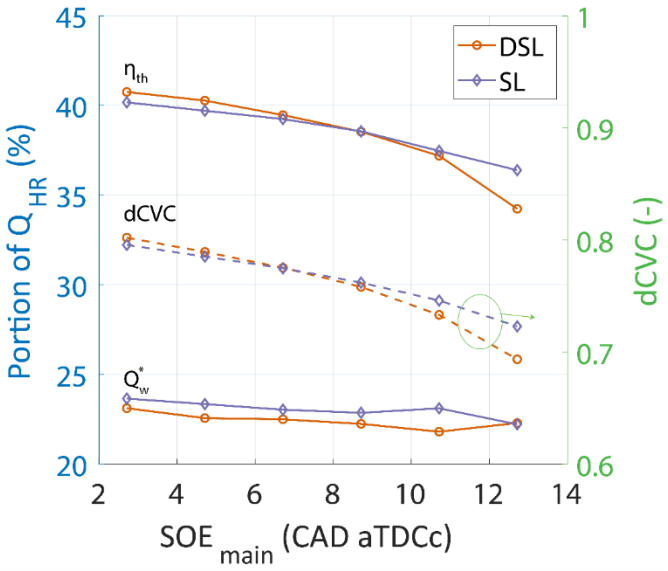

Figure 18. Thermal efficiency and degree of constant volume combustion s function of main injection timing. At near-TDC injection timing, the DSL piston has a 1.4% relative thermal efficiency gain compared to the SL piston, and higher degree of constant volume combustion.

Smoke and NOx emissions are shown in Figure 19 for operation with the DSL and the SL pistons. At the earliest, most efficient injection timing, the engine produces 69% more smoke with the DSL piston than with the baseline SL piston. As injection timing is retarded, both pistons result in decreasing smoke emissions. At the latest injection timing of 12.7 CAD aTDCc, the smoke emissions increased again for the DSL piston. NOx emissions are largely unaffected by piston geometry until the latest injection timing of 12.7 CAD aTDCc, where NOx is reduced with the DSL piston. These increased soot emissions observed with the DSL piston are a repeatable finding that is contrary to the hypothesis that stronger vortices will improve air utilization and reduce soot emissions. The reasons for this observation are not yet understood, but one possibility is the change in fuel splitting that the DSL piston creates: more fuel will be directed upward in the squish region of the DSL combustion chamber than of the SL combustion chamber. There may be a limit to the amount of fuel that can be fully oxidized in that region. Future studies will include the improved DSL piston design shown in **Error! Reference source not found.**, as well as variations of spray targeting to investigate the effects of changing fuel splitting. In addition, combustion CFD simulations will be performed to study where soot is being formed in the combustion chamber.

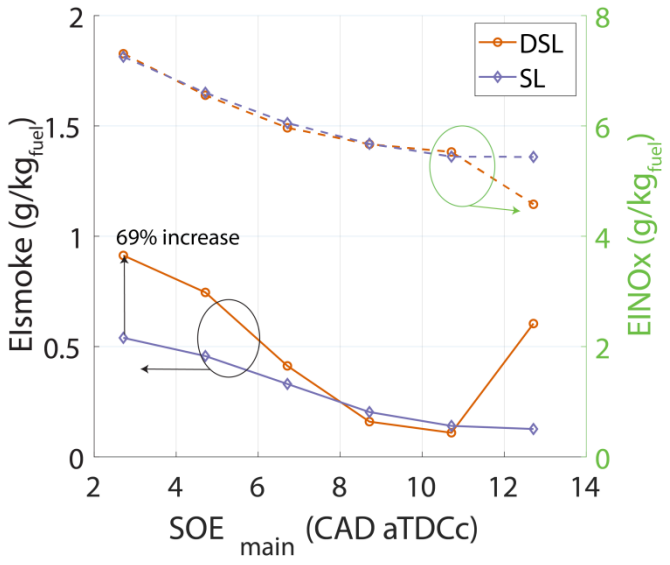

Figure 19. Smoke and NOx emission as function of main injection timing. At near-TDC injection timing, smoke emissions with the DSL piston is increased by 69% compared to the SL piston, while NOX emissions is unaffected.

Conclusions

This study features CFD simulations and experimental studies to compare the performance of two piston bowl designs in a medium-duty research engine. The production stepped-lip piston is compared against a dimpled stepped-lip piston. The simulations show that:

1. Spray-wall interactions in the step region result in strong adverse pressure gradients near the cylinder head and piston surface. The misalignment of these regions with the spray's outward momentum enable spray penetration into the squish region. By advancing injection timing towards TDC, the space in the squish region is decreased, bringing these regions of adverse pressure gradients closer to one another and acting to impede penetration into the squish region.
2. Introducing dimples with the dimpled stepped-lip piston design helps restore the separation between the regions of strong adverse pressure gradients, allowing for stronger outward radial acceleration at the near-TDC injection timing.
3. The adverse pressure gradient near the piston surface is stronger with the dimpled stepped-lip bowl than with the conventional stepped-lip piston, leading to stronger inward acceleration at the bottom of the spray. This combined with the stronger outward acceleration along the center of the spray leads to a stronger clockwise recirculating flow in the squish region of the DSL piston. This helps to produce larger, more rotationally energetic clockwise vortices in the squish region in the DSL piston than those produced in the SL piston at near-TDC injection timing.
4. Clockwise, negative vorticity is generated in the shear layer when the spray impinges on the bowl rim and is convected into the squish region. The magnitude of this vorticity is

larger in the DSL piston and is associated with stronger clockwise vortices.

5. A sensitivity study shows that to produce stronger and larger vortices at near-TDC injection timing, DSL pistons should be designed with shallower dimples, steeper curvatures, and located further into the squish region. Such an improved DSL bowl is predicted to improve rotational energy by 44%, with 27% larger total volume of the squish-region vortices compared to the baseline DSL bowl.

A piston has been produced with the baseline DSL bowl and used in single-cylinder engine experiments. Initial experiments at a part-load operating point demonstrate that:

1. The baseline DSL piston results in thermal efficiency gains of 1.4% relative to the efficiency achieved with the baseline SL piston, with a higher degree of constant volume combustion and faster mixing-controlled heat release.
2. The DSL bowl results in soot emissions that are increased by 69% at the near-TDC injection timing, but with little change in NOx emissions. Future experiments and simulations will provide further insight into the effects of DSL geometry and spray targeting on this observation.

Contact Information

Angela Wu
angwu@sandia.gov

Acknowledgments

Sandia National Laboratories is a multimission laboratory managed and operated by National Technology and Engineering Solutions of Sandia, LLC., a wholly owned subsidiary of Honeywell International, Inc., for the U.S. Department of Energy's National Nuclear Security Administration under contract DE-NA-0003525. The views expressed in the article do not necessarily represent the views of the U.S. Department of Energy or the United States Government.

Tim Gilbertson and Kent Smith are thanked for providing technical support for the engine experiments and for the fabrication of the DSL piston. The authors would like to thank Eric Kurtz at Ford Motor Company for productive discussions about the piston bowl designs and for providing the piston blanks used to produce the DSL piston. The authors would also like to thank …. for their help in reviewing and refining the manuscript.

Nomenclature

aSOEmain	After start of energizing of the main injection
aTDCc	After top-dead center compression
CAD	Crank angle degrees
CA50	Crank angle where 50% of heat is released
CFD	Computational fluid dynamics
dCVC	Degree of constant volume combustion
DSL	Dimpled stepped-lip
ECN	Engine Combustion Network
EINOx	NOx emissions index
EIsmoke	Smoke emissions index
EVO	Exhaust valve opening
$IMEP_n$	Net indicated mean effective pressure
MFB	Mass fraction burned
RPM	Revolutions per minute
SL	Stepped-lip
SOE	Start of energizing
SOI	Start of injection
TDC	Top-dead center
d_o	Dimple depth
d	Offset distance
k	Radial steepness
o	Azimuthal order
x_c	Horizontal location of midway point of the dimple sigmoid curve
n_{holes}	Number of injector holes
z_{SL}	Stepped-lip piston vertical profile
z_{DSL}	Dimple stepped-lip piston vertical profile
Q_{HR}	Integrated heat release
Q_{wall}	Wall heat transfer
Q_{LHV}	Lower heating value
W_i	Indicated boundary work over entire cycle
γ	Ratio of specific heats

P	Cylinder pressure
V	Cylinder volume
θ	Crank angle degree
A	Combustion chamber surface area
$h_{Woschni}$	Corrective heat transfer coefficient
C_m	Woschni tuning parameter
C_1	Motored velocity scale factor
C_2	Combustion-induced velocity scale factor
T_{cyl}	Bulk gas temperature
T_{wall}	Wall temperature
N	Engine speed in revolutions per second
M	Engine speed in revolutions per CAD
B	Bore
S	Stroke
P_{mot}	Motored pressure trace
v_{piston}	Mean piston speed
R_s	Swirl ratio
η_{comb}	Combustion efficiency
η_{th}	Thermal efficiency
η_{Otto}	Otto cycle efficiency
$\dot{m}_{exhaust}$	Exhaust mass flow rate
m_{fuel}	Measured fuel mass per cycle
$\dot{m}_{fuel}$	Fuel mass flow rate
y	Mass fraction
r_c	Compression ratio
V	Cylinder volume
V_d	Displacement volume
V_c	Clearance volume
Φ	Equivalence ratio
u	Velocity vector
u_x, u_y, u_z	Cartesian velocity components
u_r, u_θ, u_z	Radial, tangential, and vertical velocity components
x,y,z	Cartesian position
r, θ,z	Radial, tangential, and vertical position
ρ	Density
p	Pressure
μ	Dynamic viscosity
τ_{ij}	Reynolds stress
t	Time
ω_θ	Toroidal vorticity
Q	Q-criterion
Ω	Vorticity tensor
S	Strain rate tensor
E_{rot}	Rotational energy
m_i	Cell mass
r_c, z_c	Rotation center of vortex core
ω_i	Angular velocity of cell
I_i	Moment of inertia of cell

References

[1] E. M. Kurtz and J. Styron, "An Assessment of Two Piston Bowl Concepts in a Medium-Duty Diesel Engine." SAE Int. J. Engines 5(2): 344-352, 2012, doi: https://doi.org/10.4271/2012-01-0423.

[2] S. Iikubo, H. Nakajima, Y. Adachi, and K. Simokawa, "Combustion Chamber Structure for Direct Injection Diesel Engine," Patent Appl. US 8156927 B2, 2012. [Online]. Available: https://patents.google.com/patent/US8156927

[3] S. Busch, F. Perini, R. Reitz, and E. Kurtz, "Effects of Stepped-Lip Combustion System Design and Operating Parameters on Turbulent Flow Evolution in a Diesel Engine." SAE Int. J. Engines 13(2): 223-240, 2020, doi: https://doi.org/10.4271/03-13-02-0016.

[4] S. Busch, K. Zha, E. Kurtz, A. Warey, and R. Peterson, "Experimental and Numerical Studies of Bowl Geometry

Impacts on Thermal Efficiency in a Light-Duty Diesel Engine." SAE Technical Paper 2018-01-0228, 2018, doi: https://doi.org/10.4271/2018-01-0228.
[5] J. G. Dolak, Y. Shi, and R. D. Reitz, "A Computational Investigation of Stepped-Bowl Piston Geometry for a Light Duty Engine Operating at Low Load." SAE Technical Paper 2010-01-1263, 2010, doi: https://doi.org/10.4271/2010-01-1263.
[6] D. Yoo, D. Kim, W. Jung, N. Kim, and D. Lee, "Optimization of Diesel Combustion System for Reducing PM to Meet Tier4-Final Emission Regulation without Diesel Particulate Filter." SAE Technical Paper 2013-01-2538, 2013, doi: https://doi.org/10.4271/2013-01-2538.
[7] F. Leach, R. Ismail, M. Davy, A. Weall, and B. Cooper, "Comparing the Effect of Fuel/Air Interactions in a Modern High-Speed Light-Duty Diesel Engine." SAE Technical Paper 2017-24-0075, 2017, doi: https://doi.org/10.4271/2017-24-0075.
[8] F. Leach, R. Ismail, M. Davy, A. Weall, and B. Cooper, "The Effect of a Stepped Lip Piston Design on Performance and Emissions from a High-Speed Diesel Engine," *Applied Energy,* vol. 215, pp. 679-689, 2018, doi: https://doi.org/10.1016/j.apenergy.2018.02.076.
[9] J. Styron, B. Baldwin, B. Fulton, D. Ives, and S. Ramanathan, "Ford 2011 6.7L Power Stroke® Diesel Engine Combustion System Development." SAE Technical Paper 2011-01-0415, 2011, doi: https://doi.org/10.4271/2011-01-0415.
[10] O. Andersson and P. Miles, "Diesel and Diesel LTC Combustion," in *Encyclopedia of Automotive Engineering*. Hoboken, NJ: Wiley & Sons, Ltd, 2014, pp. 1-36.
[11] K. Nishida, T. Hashizume, R. Hasegawa, and T. Ogawa, "Low Cooling Losses and Low Emission Analysis of Small Bore Diesel Engine Combustion." SAE Technical Paper 2015-01-1824, 2015, doi: https://doi.org/10.4271/2015-01-1824.
[12] H. S. Fridriksson, M. Tuner, O. Andersson, B. Sunden, H. Persson, and M. Ljungqvist, "Effect of Piston Bowl Shape and Swirl Ratio on Engine Heat Transfer in a Light-Duty Diesel Engine." SAE Technical Paper 2014-01-1141, 2014, doi: https://doi.org/10.4271/2014-01-1141.
[13] J. Crosse, "Going Clean Off-Highway," vol. Q2, ed: Ricardo Quarterly Review, 2010, pp. 16-21.
[14] A. Smith, "Ricardo Low Emissions Combustion Technology Helps JCB Create the Off-Highway Industry's Cleanest Engine," ed. Shoreham-by-Sea UK: Ricardo, 2010.
[15] J. Lee, S. Lee, J. Kim, and D. Kim, "Bowl Shape Design Optimization for Engine-Out PM Reduction in Heavy Duty Diesel Engine." SAE Technical Paper 2015-01-0789, 2015, doi: https://doi.org/10.4271/2015-01-0789.
[16] G. D. Neely, S. Sasaki, and H. Sono, "Investigation of Alternative Combustion Crossing Stoichiometric Air Fuel Ratio for Clean Diesels." SAE Technical Paper 2007-01-1840, 2007, doi: https://doi.org/10.4271/2007-01-1840.
[17] X. Li, Z. Sun, W. Du, and R. Wei, "Research and Development of Double Swirl Combustion System for a DI Diesel Engine," *Combustion Science and Technology,* vol. 182, no. 8, pp. 1029-1049, 2010, doi: https://doi.org/10.1080/00102200903544271.
[18] K. Zha, S. Busch, A. Warey, R. C. Peterson, and E. Kurtz, "A Study of Piston Geometry Effects on Late-Stage Combustion in a Light-Duty Optical Diesel Engine Using Combustion Image Velocimetry." SAE Int. J. Engines 11(2018-01-0230): 783-804, 2018, doi: https://doi.org/10.4271/2018-01-0230.
[19] S. Busch *et al.*, "Bowl Geometry Effects on Turbulent Flow Structure in a Direct Injection Diesel Engine." SAE Technical Paper 2018-01-1794, 2018, doi: https://doi.org/10.4271/2018-01-1794.
[20] R. Cornwell and F. Conicella, "Direct Injection Diesel Engines," Patent Appl. 8770168 B2, 2014. [Online]. Available: https://patents.google.com/patent/US20130036998A1/en
[21] T. Eder, P. Lückert, M. Kemmner, and H. Sass, "OM 654 — Launch of a New Engine Family by Mercedes-Benz," vol. 77, ed: MTZ Worldwide, 2016, pp. 60-67.
[22] A. Appukuttan, J. Bisht, K. Kaundabalaraman, and H. Rathi, "Piston Bowl Design Optimization to Improve Low End Rated Torque in BS-VI Diesel Engine Based on Multi-Dimensional Combustion Simulation." SAE Technical Paper 2020-01-0241, 2020, doi: https://doi.org/10.4271/2020-01-0241.
[23] N. H. Cho, C. D. Gaikwad, N. Choudhary, and A. Sharma, "Piston with Soot Reducing Piston Bowl," Patent Appl. US 2019/0136794 A1, 2019. [Online]. Available: https://patents.google.com/patent/US10731600B2/en
[24] A. Volvo, "Technology Award for Wave Piston Design that Lowers Fuel Consumption," ed, 2017.
[25] J. Eismark, M. Andersson, M. Christensen, A. Karlsson, and I. Denbratt, "Role of Piston Bowl Shape to Enhance Late-Cycle Soot Oxidation in Low-Swirl Diesel Combustion." SAE Int. J. Engines 12(3): 233-249, 2019, doi: https://doi.org/10.4271/03-12-03-0017.
[26] G. Belgiorno *et al.*, "Experimental Study of Additive-Manufacturing-Enabled Innovative Diesel Combustion Bowl Features for Achieving Ultra-Low Emissions and High Efficiency." SAE Technical Paper 2020-037-0003, 2020, doi: https://doi.org/10.4271/2020-37-0003.
[27] W. Su and X. Zhang, "Mixing Enhancement by a Bump Ring in a Combustion Chamber for Compound Combustion." SAE Technical Paper 2005-01-3721, 2005, doi: https://doi.org/10.4271/2005-01-3721.
[28] S. Deraad *et al.*, "The New Ford 6.7L V-8 Turbocharged Diesel Engine." SAE Technical Paper 2010-01-1101, 2010, doi: https://doi.org/10.4271/2010-01-1101.
[29] F. Perini and R. D. Reitz, "FRESCO - An Object-Oriented, Parallel Platform for Internal Combustion Engine Simulations," in *28th International Multidimensional Engine Modeling User's Group Meeting at the SAE Congress*, Detroit, MI, 2018.
[30] F. Perini, K. Zha, S. Busch, and R. Reitz, "Comparison of Linear, Non-Linear and Generalized RNG-Based k-epsilon Models for Turbulent Diesel Engine Flows." SAE Technical Paper 2017-01-0561, 2017, doi: https://doi.org/10.4271/2017-01-0561.
[31] Z. Han and R. D. Reitz, "A Temperature Wall Function Formulation for Variable-Density Turbulent Flows with Application to Engine Convective Heat Transfer Modeling," *Int. J. Heat Mass Transfer,* vol. 40, no. 3, pp. 613-625, 1997, doi: https://doi.org/10.1016/0017-9310(96)00117-2.
[32] M. Jia, E. Gingrich, H. Wang, Y. Li, J. B. Ghandhi, and R. D. Reitz, "Effect of Combustion Regime on In-Cylinder Heat Transfer in Internal Combustion Engines," *Int. J. Engine Research,* vol. 17, no. 3, pp. 331-346, 2016, doi: https://doi.org/10.1177/1468087415575647.
[33] F. Perini and R. D. Reitz, "Improved Atomization, Collision and Sub-Grid Scale Momentum Coupling Models

for Transient Vaporizing Engine Sprays," *Int. J. Multiphase Flow,* vol. 79, pp. 107-123, 2016, doi: https://doi.org/10.1016/j.ijmultiphaseflow.2015.10.009.

[34] E. C. Network. "ECN Data Search Page." https://ecn.sandia.gov/ecn-data-search/ (accessed 08/01/2021.

[35] S. Busch, "Light-Duty Diesel Combustion," in *DOE Vehicle Technologies Office and Hydrogen and Fuel Cells Program Annual Merit Review*, Washington, DC, June 6 2017. [Online]. Available: https://energy.gov/eere/vehicles/downloads/vehicle-technologies-office-merit-review-2017-light-duty-diesel-combustion. [Online]. Available: https://energy.gov/eere/vehicles/downloads/vehicle-technologies-office-merit-review-2017-light-duty-diesel-combustion.

[36] F. Perini, S. Busch, E. Kurtz, A. Warey, R. C. Peterson, and R. Reitz, "Limitations of Sector Mesh Geometry and Initial Conditions to Model Flow and Mixture Formation in Direct-Injection Diesel Engines." SAE Technical Paper 2019-01-0204, 2019, doi: https://doi.org/10.4271/2019-01-0204.

[37] S. Busch, A. Wu, and S. Cho, "Catalyst-Heating Operation in a Medium-Duty Diesel Engine: Operating Strategy Calibration, Fuel Reactivity, and Fuel Oxygen Effects." SAE Technical Paper 2021-01-1182, 2021, doi: https://doi.org/10.4271/2021-01-1182.

[38] J. Somhorst, M. Oevermann, M. Bovo, and I. Denbratt, "A Method to Evaluate the Compression Ratio in IC Engines with Porous Thermal Barrier Coatings." SAE Technical Paper 2018-01-1778, 2018, doi: https://doi.org/10.4271/2018-01-1778.

[39] J. B. Heywood, *Internal Combustion Engine Fundamentals*. New York: McGraw-Hill Inc., 1988.

[40] J. Dernotte, J. E. Dec, and C. Ji, "Energy Distribution Analysis in Boosted HCCI-like / LTGC Engines - Understanding the Trade-Offs to Maximize the Thermal Efficiency." SAE Int. J. Engines 8(3): 956-980, 2015, doi: https://doi.org/10.4271/2015-01-0824.

[41] G. Woschni, "A Universally Applicable Equation for the Instantaneous Heat Transfer Coefficient in the Internal Combustion Engine." SAE Technical Paper 670931, 1967, doi: https://doi.org/10.4271/670931.

[42] J. C. R. Hunt, A. A. Wray, and P. Moin, "Eddies, Streams, and Convergence Zones in Turbulent Flows," in *Proceedings of the Summer Program*, 1988: Center for Turbulence Research.

[43] Y. Dubief and F. Delcayre, "On Coherent-Vortex Identification in Turbulence," *J. Turbulence,* vol. 1, 2000, doi: https://doi.org/10.1088/1468-5248/1/1/011.

[44] W. Qin, M. Xie, M. Jia, T. Wang, and D. Liu, "Large Eddy Simulation of In-Cylinder Turbulent Flows in a DISI Gasoline Engine," *Applied Mathematical Modelling,* vol. 38, pp. 5967-5985, 2014, doi: https://doi.org/10.1016/j.apm.2014.05.004.

[45] E. Baum, B. Peterson, C. Surmann, D. Michaelis, B. Böhm, and A. Dreizler, "Investigation of the 3D Flow Field in an IC Engine Using Tomographic PIV," *Proceedings of the Combustion Institute,* vol. 34, no. 2, pp. 2903-2910, 2013, doi: https://doi.org/10.1016/j.proci.2012.06.123.